Final Report

Development of the Electron Drift Instrument (EDI) for Cluster

NAS5-30744

13 April, 2001

Prepared by Jack Quinn
Space Science Center, Morse Hall
University of New Hampshire
Durham, NH 03824

jack.quinn@unh.edu

Table of Contents

Summary of EDI Development

The Electron Drift Instrument (EDI) is a new technique for measuring electric fields in space by detecting the effect on weak beams of test electrons. This U.S. portions of the technique, flight hardware, and flight software were developed for the Cluster mission under this contract. Dr. Goetz Paschmann of the Max Planck Institute in Garching, Germany, was the Principle Investigator for Cluster EDI.

Hardware for Cluster was developed in the U.S. at the University of New Hampshire, Lockheed Palo Alto Research Laboratory, and University of California, San Diego.

The Cluster satellites carrying the original EDI instruments were lost in the catastrophic launch failure of first flight of the Arianne-V rocket in 1996. Following that loss, NASA and ESA approved a rebuild of the Cluster mission, for which all four satellites were successfully launched in the Summer of 2000.

Limited operations of EDI were also obtained on the Equator-S satellite, which was launched in December, 1997. A satellite failure caused a loss of the Equator-S mission after only 5 months, but these operations were extremely valuable in learning about the characteristics and operations of the complex EDI instrument.

The Cluster mission, satellites, and instruments underwent an extensive on-orbit commissioning phase in the Fall of 2000, carrying over through January 2001. During this period all elements of the instruments were check and careful measurements of inter-experiments interferences were made.

EDI is currently working exceptionally well in orbit. Intitial results verify that all aspects of the instrument are working as planned, and returning highly valuable scientific information. The first two papers describing EDI on-orbit results have been submitted for publication in April, 2001, (Quinn et al., 2001; and Paschmann et al., 2001).

The principles of the EDI technique, and its implementation on Cluster are described in two papers by Paschmann et al., attached as Appendices A and B. The EDI presentation at the formal Cluster Commissioning Review, held at ESA Headquarters in Paris, is attached as Appendix C.

REFERENCES

Paschmann, G., F. Melzner, R. Frenzel, H. Vaith, P. Parrigger, U. Pagel, O.H. Bauer, G. Haerendel, W. Baumjohann, N. Sckopke, R.B. Torbert, B. Briggs, J. Chan, K. Lynch, K. Morey, J.M. Quinn, D. Simpson, C. Young, C.E. McIlwain, W. Fillius, S.S. Kerr, R. Maheu, and E.C. Whipple, The electron drift instrument for Cluster, Space Sci. Rev., 79, 233, 1997.

Paschmann, G., C.E. McIlwain, J.M. Quinn, R.B. Torbert, and E.C. Whipple, The electron drift technique for measuring electric and magnetic fields, *Measurement Techniques in Space Plasmas: Fields*, Geophysical Monograph 103, Am. Geophys. Union, 1998.

Paschmann, G., N. Sckopke, H. Vaith, J.M. Quinn, O.H. Bauer, W. Baumjohann, W. Fillius, G. Haerendel, S.S. Kerr, C.A. Kletzing, K. Lynch, C.E. McIlwain, R.B. Torbert, and E.C. Whipple, EDI electron gyro time measurements on Equator-S, Ann. Geophysicae, 17, 1513 1999.

Paschmann, G., J.M. Quinn, R.B. Torbert, H. Vaith, C.E. McIlwain, G. Haerendel, O.H. Bauer, T. Bauer, W. Baumjohann, W. Filliius, M. Foerster, S. Frey, S.S. Kerr, C.A. Kletzing, P. Puhl-Quinn, and E.C. Whipple, The electron drift instrument on Cluster: overview of first results, submitted Ann. Geophysicae, 2001.

Quinn, J.M., C.E. McIlwain, G. Haerendel, F. Melzner, D. Cauffman, Measurement of vector electric fields using electron test particles, Trans. Am. Geophys. Union, EOS, 60, 918, 1979.

Quinn, J.M., G. Paschmann, N. Sckopke, V.K. Jordanova, H. Vaith, O.H. Bauer, W. Baumjohann, W. Fillius, G. Haerendel, S.S. Kerr, C.A. Kletzing, K. Lynch, C.E. McIlwain, R.B. Torbert, E.C. Whipple, EDI convection measurements at 5-6 RE in the post-midnight region, Ann. Geophysicae, 17, 1503, 1999.

Quinn, J.M, G. Paschmann, R.B. Torbert, H. Vaith, C.E. McIlwain G. Haerendel O. Bauer, T. Bauer, W. Baumjohann , W. Fillius, M. Foerster, S. Frey, E. Georgescu, S.S. Kerr, C.A. Kletzing, H. Matsui, P. Puhl-Quinn, E.C. Whipple , Cluster EDI convection measurements across the high-latitude plasma sheet boundary at midnight, submitted Ann. Geophysicae, 2001.

Vaith, H., R. Frenzel, G. Paschmann, and F. Melzner, Electron gyro time measurement technique for determining electric and magnetic fields, in Measurement Techniques in Space Plasmas: Fields, Pfaff, Borovsky, and Young (eds), Geophysical Monograph 103, 47, American Geophysical Union, 1998.

THE ELECTRON DRIFT INSTRUMENT FOR CLUSTER

G. PASCHMANN, F. MELZNER, R. FRENZEL, H. VAITH, P. PARIGGER, U. PAGEL, O. H. BAUER, G. HAERENDEL, W. BAUMJOHANN and N. SCOPKE
Max-Planck-Institut für extraterrestrische Physik, 85740 Garching, Germany

R. B. TORBERT, B. BRIGGS, J. CHAN, K. LYNCH and K. MOREY
University of New Hampshire, Durham, NH 03824, U.S.A.

J. M. QUINN, D. SIMPSON and C. YOUNG
Lockheed Space Science Laboratory, Palo Alto, CA 94304, U.S.A.

C. E. McILWAIN, W. FILLIUS, S. S. KERR and R. MAHIEU
University of California at San Diego, La Jolla, CA 92093, U.S.A.

E. C. WHIPPLE
University of Washington, Seattle, WA 98195-1650, USA

(Received 2 May, 1996)

Abstract. The Electron Drift Instrument (EDI) measures the drift of a weak beam of test electrons that, when emitted in certain directions, return to the spacecraft after one or more gyrations. This drift is related to the electric field and the gradient in the magnetic field, and these quantities can, by use of different electron energies, be determined separately. As a by-product, the magnetic field strength is also measured. The present paper describes the scientific objectives, the experimental method, and the technical realization of the various elements of the instrument.

1. Introduction

To achieve the objectives of the Cluster program, it will be necessary to make sensitive and accurate measurements of the relevant electrodynamical parameters. The electric field is one of the essential quantities, yet it is one of the most difficult to measure. This is because in many important circumstances the electric fields are very small (less than 1 mV m^{-1}) and the plasma is very dilute, with densities less than 10 cm^{-3}. Under such circumstances, it is often difficult for the conventional double-probe technique to distinguish natural fields from those induced by spacecraft wakes, photoelectrons, and sheaths.

The instrument described in this paper is based upon the electron drift technique. This method involves sensing the drift of a weak beam of test electrons emitted from small guns mounted on the spacecraft. When emitted in certain directions, the electron beam returns to dedicated detectors on the spacecraft after one or more gyrations. During these gyrations, the beam probes the ambient electric field at a distance of some kilometers from the spacecraft, and therefore essentially outside the latter's influence. The operational principle was originally proposed by F. Melzner and was proven on ESA's GEOS spacecraft (Melzner *et al.*, 1978).

In the GEOS application the electron drift was measured only once per spacecraft revolution, and only for a restricted range of directions. These restrictions are

Space Science Reviews **79:** 233–269, 1997.

removed in the instrument described here. Two electron guns are used, each of which can be aimed electronically in any direction over more than a hemisphere. A servo loop continuously re-aims the electron guns so that the beams return to the detectors. The electron drift can be calculated by triangulation of the two emission directions. This method was developed by McIlwain and Quinn at UCSD and proposed for NASA's Equator mission. Comparing the drifts of electrons emitted at different energies enables electric fields and magnetic field gradients to be determined separately.

For small magnetic fields, the triangulation method becomes inaccurate, and the drift will instead be calculated from the differences in the time of flight of the electrons in the two nearly oppositely directed beams. This technique was developed by Tsuruda at ISAS and is being employed on the NASA/ISAS Geotail mission (Tsuruda *et al.*, 1985). The time-of-flight measurements also yield an accurate determination of the magnetic field strength.

The electron drift technique has a number of limitations. First, the measurements will be interrupted whenever electrons are strongly scattered by instabilities or interactions with ambient fluctuations. Second, beam tracking will be disrupted by very rapid changes in either the magnetic or the electric field. Third, accurate separation of the electric and magnetic components of the drift may not always be possible with only a limited range of electron energies.

From the respective strengths and weaknesses of the electron drift and double-probe techniques, it is quite obvious that they complement, rather than replace, each other.

The present paper is an expanded version of that published earlier (Paschmann *et al.*, 1993).

2. Scientific Objectives

The ability of the EDI instrument to make accurate and highly sensitive measurements of the electric field and of the perpendicular gradient of the magnetic field makes possible a variety of studies that comprise the essence of the Cluster mission.

Cluster has been designed primarily to study small-scale structures in three dimensions in the Earth's plasma environment. Although they are of relatively small scale, the processes leading to the formation of such structures are believed to be fundamental to the key processes of interaction between the solar wind and the magnetospheric plasmas. We refer the reader to the companion papers for an account of the Cluster objectives (Escoubet *et al.*, 1996, this issue, for example).

Table I lists the quantities that can be obtained from the measured electric fields and magnetic field gradients, and the information that can be derived. One of the prime objectives of the Cluster mission is to obtain differential quantities by measurements of particle and field properties at the four spacecraft locations. These differences can be used to form quantities such as the gradient, curl, and

Table I
Derivable information

Tools	Information
$\mathbf{E}^i + (\mathbf{v}^i \times \mathbf{B}^i)$	Resistivity; deviation from frozen flux condition
$\mathbf{E}^i \cdot \mathbf{I}$	Conversion of electromagnetic energy
Variance analysis of $\mathbf{E}^i(t)$	Attitude and motion of boundaries; normal and tangential fields
Least-squares fit of $\mathbf{E}^i(t)$	deHoffmann–Teller frame; intrinsic electric fields
$\int_{t_1}^{t_2} \mathbf{E}^i(t) \cdot \mathbf{u}\, dt$	Potential difference across layer or discontinuity
$\int_{t_1}^{t_2} \nabla_\perp B^i(t) \cdot \mathbf{u}\, dt - [B^i(t_2) - B^i(t_1)]$	Measure of stationarity of magnetic field profiles
$\nabla_\perp B^i(t) \cdot \mathbf{s}^{ij} - [B^j(t) - B^i(t)]$	Comparison of small and large-scale magnetic gradients
$\langle E_x^i(t) E_y^j(t+\tau) \rangle$	From this and other correlations: characterization of turbulence
$\nabla \cdot \mathbf{E}$	Shear flows
$\nabla \times \mathbf{E}$	$\partial \mathbf{B}/\partial t$; induction electric fields

Superscripts i, j indicate the four spacecraft locations.
$\mathbf{u}$ denotes boundary velocity, $\mathbf{s}^{ij}$ denotes inter-spacecraft separation.
Vector derivatives are approximated by finite differences between quantities measured at the different spacecraft locations.

divergence of the fields, and of the plasma moments such as velocity and pressure. These differentials will yield other physical properties such as current densities from $\nabla \times \mathbf{B}$, vorticity flow from $\nabla \times \mathbf{v}$, shear flows from $\nabla \cdot \mathbf{E}$, induction electric fields from $\nabla \times \mathbf{E}$, and momentum balance from the divergence of the pressure and magnetic stress tensors.

EDI can be used to obtain the magnetic field gradient in the plane perpendicular to the magnetic field, $\nabla_\perp B$. This will be a useful supplement to the differentials obtained from measurements made at the four spacecraft. The spacecraft separation will in general be much larger (hundreds of km) than the electron gyroradius (a few to tens of km) which is the scale on which EDI will measure $\nabla_\perp B$. Comparing the two differentials will allow a test of the consistency of the differentials over the two scales.

2.1. Bow Shock

The electric field plays a very important role in the physics of collisionless shocks. In a laminar shock, the electrons are magnetized and follow equipotentials, while the ions are unmagnetized and are decoupled from the electrons because of the inertia. Charge separation occurs, which causes an electric field along the shock normal, which in turn slows down the ion population. How this electric field is distributed in the shock layer is almost completely unknown.

Combining our measurements of $\nabla_\perp B$ with the larger-scale field gradients obtained from the magnetometer records on the four spacecraft will help to assess

the stationarity of the magnetic field profiles across the shocks. Our $\nabla_{\perp} B$ measurements are also important in determining the occurrence of the so-called isomagnetic jumps in electric potential across the shock layer.

An important question about the Earth's bow shock is what mechanisms provide the required dissipation in the absence of particle collisions. It is known that some dissipation is provided by the coherent reflection of a fraction of the incident ion population, especially for quasi-perpendicular shocks. The ion distributions are also subject to instabilities leading to waves which scatter particles. Under quasi-parallel geometries there is coupling between reflected and incident particles. This coupling can lead to large-amplitude turbulence. Fast electric and magnetic field measurements at the four Cluster locations will permit a description of the low-frequency turbulence that is an important means of dissipating the solar-wind energy at the shock. The measurement of **k** vectors together with fast plasma measurements will make it possible to determine the wave modes and also the wave-particle interaction mechanisms. Shock surface waves can also be studied in this way.

2.2. MAGNETOPAUSE, BOUNDARY LAYER, AND POLAR CUSP

The magnetopause is an example of a current sheet formed when two magnetized plasmas interact with each other. In the simplest physical picture, in which the magnetic fields are frozen into the plasma, the two interacting plasmas remain separate. Therefore the major interest is in those processes that violate the frozen flux condition and then lead to transfer of mass, momentum and energy across the current sheet.

Violation of the frozen flux theorem implies that the measured electric field, $\mathbf{E}$, differs from the convection electric field, $\mathbf{E}_c = -(\mathbf{v} \times \mathbf{B})$. Such differences will reveal contributions from the resistive term and the Hall current term in the generalized Ohm's law. The search for cases with $\mathbf{E}_c \neq \mathbf{E}$ will therefore be one of the prime objectives of this investigation.

Comparison can also be made with the fields computed from the deHoffmann–Teller transformation velocity. The electric field in the spacecraft frame may be approximated by $\mathbf{E}_{\mathrm{HT}} = -(\mathbf{v}_{\mathrm{HT}} \times \mathbf{B})$ where $\mathbf{v}_{HT}$ is the velocity of the deHoffmann–Teller frame in which the electric field vanishes. Systematic differences between $\mathbf{E}_c$ and $\mathbf{E}_{\mathrm{HT}}$ may reveal details concerning the magnetopause structure, such as the existence of an intrinsic electric field component normal to the layer.

Processes that lead to such deviations are expected to operate only on small spatial scales. In magnetic reconnection, for example, there is the diffusion region around the X-line which separates the regions of different magnetic field topology. But reconnection also implies the presence of non-zero electric fields, E_t, tangential to the magnetopause over much larger scales. Because E_t is necessarily rather small (of the order of 1 mV m^{-1}), it has not been measured in the past except in a few cases. Most of the previous in-situ evidence for reconnection at the magnetopause has

come from measurement of high-speed plasma flows, which give no information on the reconnection rate. Thus the systematic measurement of E_t and its spatial scale remains one of the outstanding tasks of the Cluster mission. In addition to such rather laminar transport processes, macroscopic and/or microscopic turbulence is expected to play an important role at the magnetopause. It therefore will be of prime importance to study the fluctuations in the electric field and their four-point correlations.

As a consequence of the transfer processes, a boundary layer of solar wind plasma exists inside the magnetopause. The significance of the various portions of the boundary layer for the transport of magnetic flux, and thus for the cross-magnetotail potential, can be assessed from measurement of the electric potential across the layer. Previous estimates relied on single-spacecraft measurements which become highly suspect in the presence of boundary motions or non-stationary conditions. The availability of measurements on the four Cluster spacecraft will go a long way towards improving the accuracy of the potential measurement.

Not only do the four-spacecraft measurements provide the means to identify the spatial scales for the transport processes, they also allow for approximate determinations of quantities such as $\nabla \times \mathbf{E}$ or $\nabla \cdot \mathbf{E}$. $\nabla \times \mathbf{E}$ is a measure of $\partial \mathbf{B}/\partial t$ and thus helps to assess temporal changes in the magnetic field configuration; $\nabla \cdot \mathbf{E}$, on the other hand, is related to shear flows and therefore complements the direct plasma-flow measurements.

For the polar-cusp region, a major objective will be the study of plasma turbulence, because eddy diffusion or turbulent convection has been invoked as the dominant plasma transport mechanism in that region. Correlations between the four spacecraft will help to confirm or deny this type of transport.

2.3. MAGNETOTAIL

The electron drift instrument will provide reliable surveys of the convection electric field in the tail, not only in the equatorial plane but also along the north-south direction where strong gradients seem to exist near the plasma sheet boundary layer. These surveys should lead to a better understanding of the entry of solar wind/lobe plasma into the central plasma sheet and the circulation of this plasma to the frontside magnetosphere.

Another important topic where electric field measurements can contribute to our understanding is that of current sheets. Current sheets in the magnetosphere, such as in the magnetotail, are critical regions in that they are the most important sites of particle energization. In these current sheets, the magnetic field is small, the gyroradius can be large compared to the scale size, and consequently the electric field can play a dominant role in the particle motion. Attention is being focussed on these regions as sites for magnetic field reconnection, where magnetic field energy can be transformed into particle kinetic energy.

Major questions about current sheets are the mechanisms for their formation and their structure, the mechanisms for dissipation and diffusion, and the mechanisms for disruption and collapse.

In self-consistent studies of the tail current sheet it has been shown that it is possible to have particles trapped in the current sheet because of the mirror geometry that arises from the existence of the minimum of the magnetic field strength at the center of the sheet (e.g., Cowley, 1978). The normal component of **E** is an important factor in this trapping since it reflects particles with the proper sign and energy and also assists in the maintenance of quasi neutrality. It is likely that these trapped populations in the central plasma sheet become accelerated to high energies by the strong inductive electric fields that are present during magnetic substorms, and it is quite probable that they eventually turn into the plasmoids that have been inferred to move with high velocities along the Earth's magnetotail during substorms (Hones, 1979). EDI will measure both the normal and tangential components of **E** in the tail sheet during quiet times in order to help to identify the trapped population there. In addition it will measure the inductive electric fields during substorms which are an important element of the acceleration processes during these events.

Since the EDI instrument will measure the electric field at up to tens of samples per second, the combined electric- and magnetic-field data is well suited for studying ultra-low frequency (ULF) waves in the range of about 10 Hz to several hundred mHz. This range covers many kinds of magnetohydrodynamic (MHD) waves as well as ion plasma waves in regions of low magnetic fields. While most earlier work was based on magnetic field data alone, the combined electric and magnetic data allow the determination of the wave's **k** vectors and Poynting fluxes. Measuring the Poynting flux simultaneously with all four spacecraft also provides a good determination of the resonance regions where wave energy is trapped on a field line in the form of standing oscillations. The ability of EDI to obtain magnetic field gradients becomes important when studying so-called drift-mirror waves which are excited due to ∇B-drifting energetic protons with large perpendicular temperatures (Baumjohann *et al.*, 1987).

The ability to infer an estimate of $\nabla \times \mathbf{E}$ from the four-spacecraft measurements will allow an assessment of temporal changes in the global magnetotail configuration during substorms.

2.4. Inner Magnetosphere

Prime objectives in the inner magnetosphere include studies of the electric fields associated with convection, ULF waves, and particle injections.

The concept of plasma convection in the magnetosphere has unified a number of high-latitude geophysical phenomena. However, there has been a paucity of direct measurements of the convection electric field in the inner (4–12 R_E) equatorial magnetosphere. Early inferences of the electric field were from ground-based

observations of plasma drifts – in the ionosphere for example – which were interpreted in terms of $\mathbf{E} \times \mathbf{B}$ drifts. These ionospheric electric fields were then mapped upwards along magnetic field lines into the magnetosphere to obtain estimates of magnetospheric electric fields.

A few electric field measurements have been reported within the plasmasphere from GEOS 1 and ISEE 1 (Pedersen *et al.*, 1978), but most measurements further out were made by the double-probe technique during substorm events when the fields were large (Aggson and Heppner, 1977; Pedersen *et al.*, 1984). Particle measurements in the equatorial region have been used to infer electric fields outside the plasmasphere (McIlwain, 1972; McIlwain, 1981), but it was not until the electron beam technique on GEOS became available that direct measurements in the outer equatorial magnetosphere during quiet times were reported (Baumjohann and Haerendel, 1985; Baumjohann *et al.*, 1985).

Plasma injections are the sudden appearances of energetic plasma at all energies and directions in the equatorial magnetosphere during magnetospheric substorms, frequently within a few tens of seconds of substorm onset (DeForest and McIlwain, 1971). The injected plasma appears to come from a well-defined injection boundary that maps down along the Earth's magnetic field lines to the equatorward edge of the auroral oval. There are probably strong electric fields associated with these plasma injections which may be transient and/or localized at the injection boundary. EDI will measure these fields, including inductive fields, with a time resolution of up to several tens of Hz at all magnetospheric activity levels; these measurements should allow analysis of the plasma motions during these events to yield a better understanding of the injection process.

There has been recent renewed interest in the convection electric field because it is now realized to be central to many magnetospheric processes, including the global MHD equilibrium, reconnection rates, Region-2 Birkeland currents, magnetosphere-ionosphere coupling, ring current and radiation belt transport, substorm injections, and several acceleration mechanisms. New algorithms have been developed to extract electric fields from particle data (Sheldon and Gaffey, 1993; Sheldon and Hamilton, 1994). It is essential, however, that these indirect techniques be supplemented by accurate, high resolution, direct measurements of the electric field of the kind that will be obtained by EDI.

2.5. SMALL-SCALE STRUCTURES

Dilute plasmas appear to have a strong tendency to create fine structure. The reasons for the formation of such small-scale structures are manifold: gradient instabilities, current bunching, heat-flux instabilities, cascading from longer wavelength turbulence, beam-plasma interactions, kink-, firehose- or flute-type instabilities. Fine structure may in fact be nature's preferred way to create dissipation. The thinness of auroral arcs testifies that the hard-to-sustain parallel electric fields are

a consequence of the fine-structuring and accompanying enhancement of electric currents.

Little is known about fine structure in such situations: their morphology (spatial scales), time scales, and amplitudes. Organization along the magnetic field direction is most frequent, but the coherence lengths (parallel wave numbers) can only be guessed. Cluster will be the first attempt to unravel the origin, dynamics and macroscopic consequences of fine structure in a cosmic plasma with a suitable tool.

The measurement of electric fields deserves special attention in such small-scale structures. Whereas $\mathbf{E}$ appears as a secondary quantity in magnetohydrodynamics, this is certainly not the case for scale lengths comparable to or smaller than the ion gyroradius. In many situations, the ions can even be regarded as unmagnetized, i.e., the electric force may dominate their dynamics. The electrons, on the other hand, perform an $\mathbf{E} \times \mathbf{B}$-drift that may contribute strongly to the electric current, in contrast to the regular current-free plasma convection on larger scales. Electric fields, electron pressure gradients and magnetic stresses are intimately related under these circumstances:

$$\mathbf{E} = \frac{1}{e\,n}\left[-\left(\nabla p_e + \nabla\frac{B^2}{2\mu_0}\right) + \frac{1}{2\mu_0}(\mathbf{B}\cdot\nabla)\mathbf{B}\right] . \tag{1}$$

The proposed electron beam technique allows a simultaneous measurement of $\mathbf{E}$ and $\nabla(B^2/2\mu_0)$, two essential quantities in the force balance. Together with measurements of the pressure tensor and of the magnetic tension with four spacecraft, one has a powerful tool for studies of the dynamics of small-scale structures.

EDI should bring a significant enhancement to the study of current sheets and filaments since it will simultaneously measure the electric and magnetic fields, and in particular the perpendicular components of the magnetic field gradient associated with these currents. For example, previous inferences of field-aligned current structures have come from magnetometer data where only the gradient of $\mathbf{B}$ along the spacecraft path was obtained. EDI will often provide gradients in the plane transverse to $\mathbf{B}$ as well as along the trajectory. This, together with electric field data, should allow a much better determination of the structure of these current systems.

3. Principle of Operation

3.1. Drift Velocity from Beam Direction Measurements

The basis of the electron drift technique is the injection of test electrons and the registration of their gyrocenter displacements after one or more gyrations in the magnetic field, $\mathbf{B}$. The displacement, $\mathbf{d}$, is related to the drift velocity, $\mathbf{v}_D$, by:

Table II
Characteristic quantities for key regions

Parameter	Solar Wind	Magneto-sheath	Cusp	Tail lobe	Plasma-sheet	Ring current
Magnetic field, B, nT	8	40	40	30	20	300
Electric field, E, mV m^{-1}	3.6	8.0	4.0	0.5	1.0	1.0
Electron gyroradius, R_g, km	13	3	3	4	5	0.4
Electron gyrotime, T_g, ms	4.5	0.9	0.9	1.2	1.8	0.1
Drift step, d, m	2000	179	89	20	89	0.4
ToF difference, ΔT, μs	214	19	9	2	9	0.04
Angle change, δ, deg	8.7	3.9	1.9	0.3	1.0	0.1
Ambient diff. E-flux	1.0×10^5	1.0×10^6	1.0×10^7	1.0×10^5	2.0×10^7	1.0×10^8
Beam current, nA	1000	200	300	30	400	1
Optics state	6	3	7	3	7	4
Ambient count rate, s^{-1}	2.1×10^4	1.6×10^4	2.2×10^5	1.6×10^3	4.4×10^5	1.4×10^5
Beam count rate, s^{-1}	7.2×10^4	3.8×10^5	3.8×10^5	5.4×10^5	3.6×10^5	2.3×10^5
Contrast	3.4	23.5	2.5	237	0.8	1.7
Signal-to-noise ratio	15.6	93.8	36.5	300	17.2	19.7

Table values are for 1 keV electrons.
Beam currents, beam count rates, contrast, and signal-to-noise ratios are for times the beams are gated on (total of 1 ms per 2 ms sample). Beam and background count rates are computed for the collection areas A and geometric factors H associated with the chosen Optics State (see Table III).

$$\mathbf{d} = \mathbf{v}_D \cdot N \cdot T_g \,, \tag{2}$$

where T_g is the gyroperiod and N denotes the number of such periods after which the electrons are captured. If the drift is solely due to an electric field, $\mathbf{E}_\perp$, transverse to $\mathbf{B}$, then (using MKSA units)

$$\mathbf{d} = \frac{\mathbf{E}\times\mathbf{B}}{B^2}\cdot N \cdot T_g \,. \tag{3}$$

Or, numerically, for $N = 1$

$$d\,(\mathrm{m}) = 3.57\times10^4\,\frac{E_\perp\,(\mathrm{mV\ m^{-1}})}{B^2\,(\mathrm{nT})}\,. \tag{4}$$

Typical values for B, $E_\perp$, the electron gyroradius and gyrotime, and the drift step d (as well as other quantities referred to later) are listed in Table II for various regions of interest. For any other choice of magnetic and electric fields, the reader is referred to Figure 1.

It is important to realize that after one gyration, all electrons emitted from a common source S in a plane normal to $\mathbf{B}$, are focussed onto a single point that is displaced from S by the drift step, $\mathbf{d}$ (Figure 2). A detector, D, placed at the focus would detect these electrons. As $\mathbf{d}$ is the quantity to be measured, it is not possible

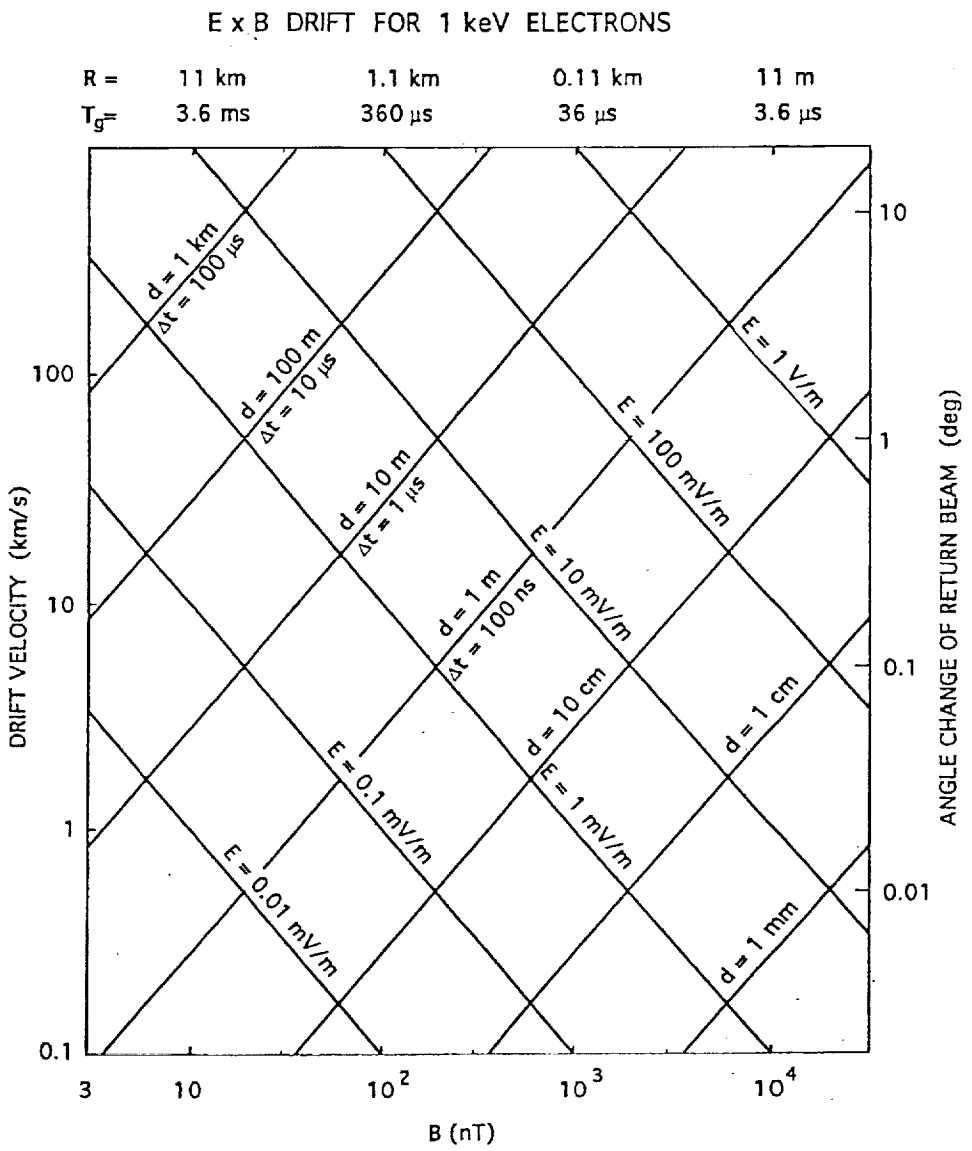

Figure 1. Drift parameters for 1 keV electrons

to put an electron source at S. Fortunately this is not necessary. A beam from an arbitrarily located electron gun will also hit the detector at D, provided the beam is directed towards S. In this case the gun can be thought of as supplying electrons to the source at S, from where they proceed to D, as described. The beam may also be directed away from S, in which case it assumes the role of a beam emanating from the source, as illustrated in Figure 2. If two guns are used, as shown in the figure, measurement of the two emission directions that return a beam onto the detector

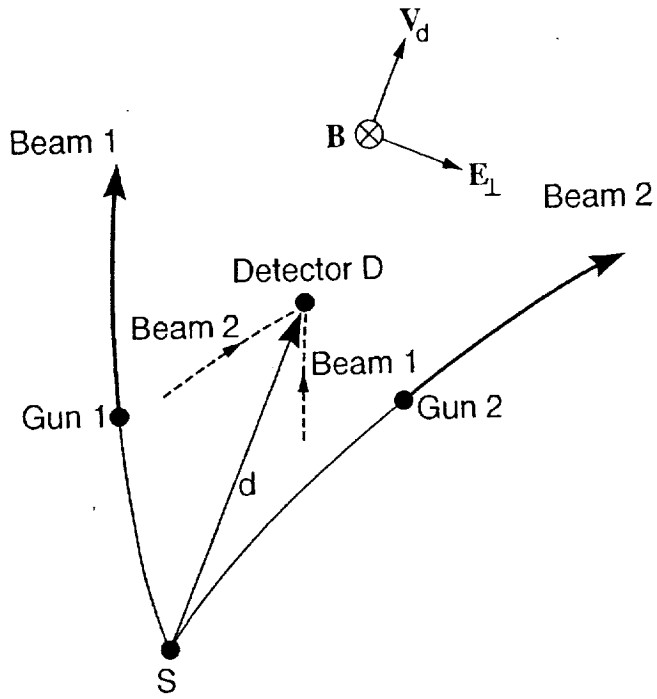

Figure 2. Principle of drift step triangulation. If as a result of the drift all electrons emitted from S reach the detector location D after one gyration, then the beams emitted from two arbitrarily placed guns will also strike the detector if they are directed along lines through S. The drift step **d** is therefore the vector from the intersection point of the two beam directions to the detector D, once the beams are steered such that an 'echo' is received by the detector.

yields the displacement, **d**, and thus the drift velocity, $\mathbf{v}_D$. This is a straightforward triangulation problem that in principle can be done continuously and with high time resolution.

Note that with guns placed at locations other than S, D is no longer a focal point of the beams, nor do the travel times precisely equal the gyrotime, T_g. If the beam is directed towards (away from) S, the travel time will be longer (shorter) than T_g. In subsequent discussions we often refer to S as the target. The angle (in radians) between outgoing and returning beam is given by

$$\delta \approx 2\pi \frac{v_D}{v} , \tag{5}$$

where v is the electron speed. For drift speeds of 100 km s^{-1} (and 1 keV electron energy), the angle δ is 1.9°, increasing to almost 10° at 500 km s^{-1}. As we will see later, a large δ complicates operation.

A solution with a single detector, as illustrated in Figure 2, is not practical, as the detector would have to detect beams from two different directions at the same time. Once two separate detectors are employed, the scheme changes from that

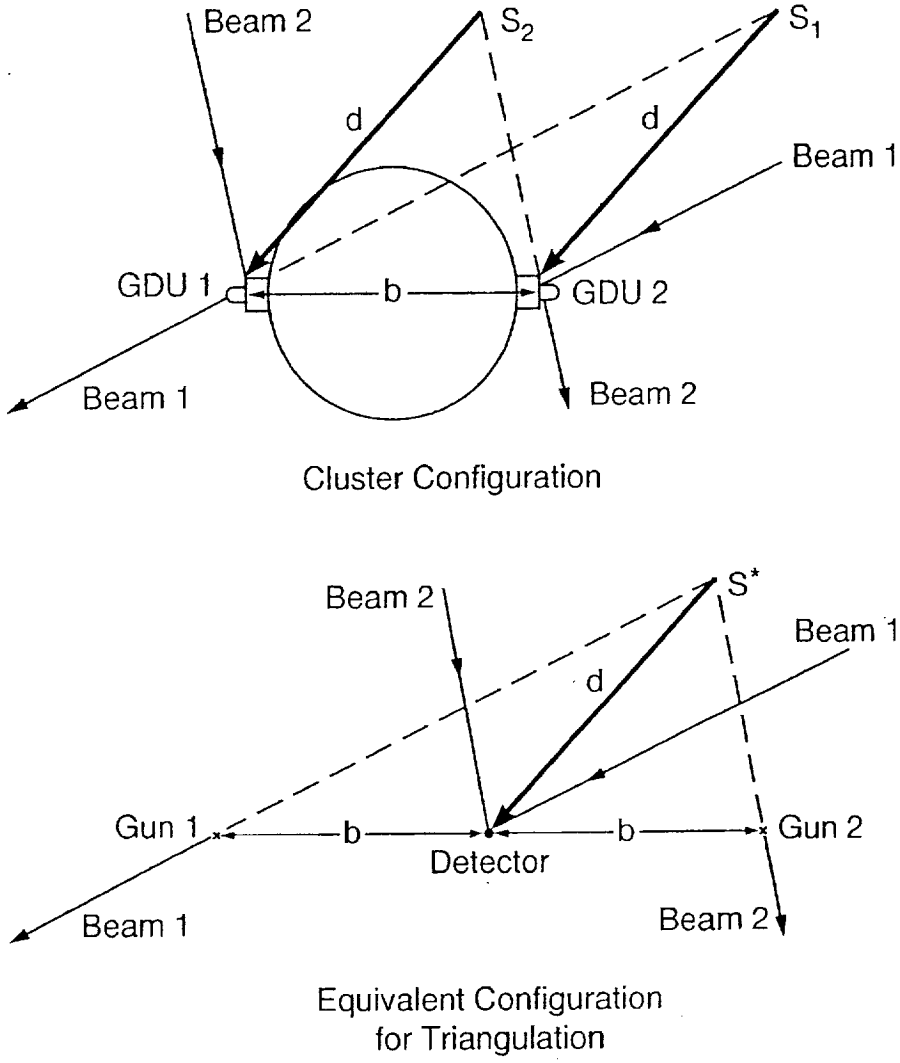

Figure 3. Triangulation scheme for two gun/detector units placed on opposite sides of the spacecraft, at a distance b (top). S_1 and S_2 are the virtual source points for the two detectors. The problem is equivalent to one with two guns spaced $2b$ apart, a single detector, and a single source point S^* (bottom).

in Figure 2 to that shown in Figure 3. Here two gun-detector units (GDU's) are placed on the spacecraft at a distance b, as shown at the top of Figure 3, as required by technical constraints on Cluster (see Section 3.6). In this case one has separate source points, S_1 and S_2, one for each detector. As far as triangulation is concerned, this configuration is equivalent to one where the two guns are spaced $2b$ apart and a single detector is placed half-way inbetween, as shown in the bottom part of Figure 3. Thus one has effectively gained a factor of 2 in triangulation baseline.

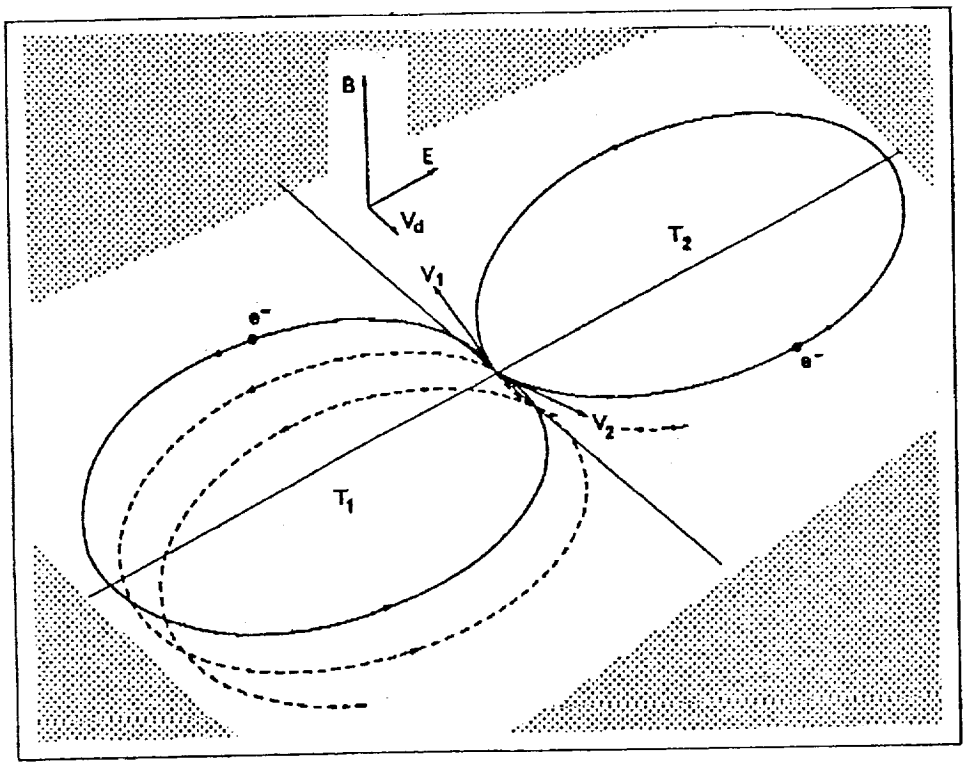

Figure 4. Principle of drift determination via time-of-flight measurements. Electrons emitted in a direction, V_1, opposing the drift, V_d, travel a longer path, and thus have a longer gyrotime, T_1, than electrons emitted along the drift, which take T_2.

As is true for any triangulation problem, the length of the baseline, b, naturally determines the precision with which the displacement, $\mathbf{d}$, can be measured. The baseline is defined as the distance transverse to $\mathbf{v}_D$ between a gun and its associated detector when projected into the plane perpendicular to $\mathbf{B}$. For the configuration with two gun-detector pairs depicted in Figure 3, the maximum effective baseline is twice the actual physical distance between the units, i.e., 6 m. Assuming 1° knowledge of the beam firing direction, one can then determine displacements up to 60 m to better than 20%.

Consulting Table II, one sees that much larger drift steps can occur. For such drift steps the triangulation technique still determines the direction of the drift with high accuracy, but not its magnitude. Under such conditions, electron time-of-flight measurements will be used to determine the magnitude of the drift step. Similarly for very small drift steps, the direction becomes uncertain.

3.2. DRIFT VELOCITIES FROM TIME-OF-FLIGHT MEASUREMENTS

Appropriate pulse-coding of the beams makes it possible to measure the time of flight of the electrons with a resolution better than 1 μs, if the magnetic field is sufficiently stable over the electron gyroperiod. As illustrated in Figure 4, electrons in the two beams returning to the detectors travel different path lengths. As a result their flight times differ by an amount given by

$$\Delta T = T_{\text{to}} - T_{\text{aw}} = 2T_g \frac{v_D}{v} \propto \frac{d}{v} ,$$

where T_{to} and T_{aw} are the flight times for the beam electrons aimed towards and away from the target, respectively. In the limit of very large drift steps, as depicted in Figure 4, the towards (away) beams are directed essentially anti-parallel (parallel) to the drift velocity. For simplicity we have assumed here that guns and detectors are collocated, or in other words, that the drift step is large compared to gun-detector separations.

Measuring T_{to} and T_{aw} permits determination of $\mathbf{v}_D$. ΔT scales directly as d/v. Hence, while the triangulation becomes increasingly less accurate, the time-of-flight method becomes more accurate with increasing drift step d, limited only by signal-to-noise effects. As shown in Table II, ΔT is 9 μs or larger (and thus accurately measurable) for those regions where the triangulation method starts to fail.

3.3. MEASUREMENT OF B

The gyroperiod itself is obtained from the mean of the travel times:

$$T_g = \frac{T_{\text{to}} + T_{\text{aw}}}{2} . \tag{7}$$

From T_g the magnetic field strength, B, is obtained via

$$T_g = \frac{2\pi m}{eB} . \tag{8}$$

Values of T_g range from about 0.1 to 10 ms (see Table II). When times of flight are measured, the magnetic field strength is determined with very high accuracy, e.g., to within 0.1% for a 30 nT field. This feature can be used for an accurate in-flight determination of the fluxgate magnetometer offsets.

3.4. SEPARATION OF ELECTRIC AND MAGNETIC GRADIENT DRIFT

The beam electrons are subject not only to electric field drifts, but also to drifts caused by magnetic field gradients, $\nabla_\perp B$, directed perpendicular to the magnetic field. When the scale-length, ℓ, of such inhomogeneities becomes small (as it does

at the bow shock, the magnetopause, or at the edges or the center of the plasma sheet), the gradient drift will make a significant contribution to the test electrons' displacement. The ratio of this drift, v_B, to that caused by the transverse electric field in the spacecraft frame of reference, v_E, is

$$\frac{v_B}{v_E} = 10^3 \frac{W_e\,(\mathrm{keV})}{E_\perp\,(\mathrm{mV\ m^{-1}})}\,\ell^{-1}\,(\mathrm{km})\,, \tag{9}$$

where W_e is the energy of the electrons. For 1 keV test electrons and a field of 1 mV m^{-1}, v_B/v_E reaches unity if ℓ approaches 1000 km. For this reason we foresee the use of electrons at different energies, typically 0.5 and 1.0 keV. A wider range of energies would help to separate the drifts but is beyond the capabilities of EDI, primarily because of limitations in gun and detector voltage supplies.

When the total drift is measured at two energies, W_1 and W_2, with $r = W_2/W_1$, the electric and magnetic drifts are obtained from the following expressions:

$$\mathbf{v}_E = \frac{(r\mathbf{v}_1 - \mathbf{v}_2)}{(r-1)}\,, \tag{10}$$

$$\mathbf{v}_B(W1) = \frac{(\mathbf{v}_2 - \mathbf{v}_1)}{(r-1)}\,, \tag{11}$$

where $\mathbf{v}_1$ and $\mathbf{v}_2$ are the (total) drifts that are inferred from the triangulation analysis applied to the two measurements at energies W_1 and W_2, respectively.

When the time-of-flight measurement technique is used in the presence of a significant gradient in **B**, the analysis is more complicated. Since the gyrotime is defined in terms of the magnetic field at the center of the gyro circle, the two beams fired parallel and anti-parallel to the drift direction (Figure 4) will have different gyro times. If there were only the $\nabla_\perp B$ drift (i.e., no electric field) then the gyro times are given by

$$T_g = T_0\left(1 + \frac{R_g \sin\Phi_0}{\ell}\right)\,, \tag{12}$$

For the anti-parallel beam, $\Phi_0 = \pi/2$ and for the parallel beam $\Phi_0 = -\pi/2$, if one assumes that the gradient in **B** is in the same direction as **E** in Figure 4. Here T_0 is the gyrotime as given by the magnetic field at the spacecraft and R_g the corresponding gyroradius. The drift velocity and drift step are:

$$v_B = v_{B0}\left(1 + \frac{2R_g \sin\Phi_0}{\ell}\right)\,, \tag{13}$$

$$d_B = d_{B0}\left(1 + \frac{3R_g \sin\Phi_0}{\ell}\right)\,, \tag{14}$$

where again v_{B0} and d_{B0} are the values in terms of the magnetic field at the spacecraft. Use of the measured times now results in

$$T_{to} + T_{aw} = 2T_0 \tag{15}$$

as before, but

$$\Delta T = T_{to} - T_{aw} = 6T_0 \frac{v_{B0}}{v_0} . \tag{16}$$

When both an electric field and a gradient in the magnetic field are present it can be shown that the difference in measured times for two beams fired anti-parallel and parallel to the net drift direction is given to leading order by

$$\Delta T = T_0 \left(4 \frac{v_{B0}}{v_0} \sin \delta\Phi + \frac{2}{v_0} |\mathbf{v}_E + \mathbf{v}_{B0}| \right) . \tag{17}$$

Here, $\delta\Phi$ is the starting angle of the anti-parallel beam with respect to the direction of the magnetic field gradient.

In general there are four unknown quantities: the magnitude and direction (or equivalently, the x and y components) of both $\mathbf{v}_B$ and $\mathbf{v}_E$ in the plane perpendicular to $\mathbf{B}$. When two energies are used there will be six measured quantities: two net drift directions (one at each energy) and two pairs of flight times for the parallel and anti-parallel beams. However, the flight times are not all independent since the sum of the pair for each energy is $2T_0$. Nevertheless the net drift directions and the differences in measured flight times for the two energies provide four relations that make it possible to obtain the four unknown drift components of $\mathbf{v}_B$ and $\mathbf{v}_E$.

3.5. Return Beam Intensities

The flux of returning beam electrons incident on the detector depends upon many factors, including the angular current distribution of the outgoing beam, the beam gyroradius, possible beam modification by electrostatic or wave-particle forces, and the geometrical arrangement of the gun and detector with respect to the drift step vector. The outgoing beam has an opening angle, α, of approximately 1°. Thus the beam diverges along the magnetic field direction by a distance $s_{||} = 2\pi R_g \alpha / 57.3$, where R_g is the gyroradius, but is focussed in the plane perpendicular to $\mathbf{B}$ after one gyro orbit. By definition, this focus is located one 'drift step' from the gun. In general, those beam electrons with the proper firing direction encounter the detector either somewhat before, or somewhat after, this focus point. Because of the angular divergence both along and perpendicular to $\mathbf{B}$, the detector intercepts only a very small part of the emitted beam.

Equation (18) gives the beam flux, F, in $\mathrm{cm}^{-2}\mathrm{s}^{-1}$, at the detector for an emitted beam with a flat current distribution over a square angular cross-section, where I is the gun current in nA, B the magnetic field strength in nT, W the beam energy in keV, x the distance from the gun's gyrofocus to the detector in m, α the beam full width parallel and perpendicular to $\mathbf{B}$ in degrees, and R_g the gyroradius in m.

$$F = 3.1 \times 10^3 \frac{IB}{x\alpha^2 W^{1/2}\,(1 \pm x/2\pi R_g)}\,. \tag{18}$$

The $\pm$-term in the denominator accounts for divergence parallel to **B** between the gun's gyrofocus and the detector, depending upon whether the detector intercepts the beam before $(-)$ or after $(+)$ the gyrofocus. Of course a square, uniform cross-section is not a realistic representation of the actual beam. However for that portion of the real beam that has the same angular current density I/α^2 as the uniform beam, the return flux at the detector would be the same.

The beam divergence leads to a large variation in the return beam flux with magnetic field intensity and drift step. In order to compensate partially for this variation, both the beam current and the detector optics are adjusted by EDI's controller unit. The optics may be commanded into a number of different 'states' (see Section 4.2). These states allow a good deal of flexibility in the choice of the detector's effective area (A) to the return beam and its geometric factor ($H = G\Delta E/E$) to ambient electrons.

Table II illustrates sample values of return-beam count rates and signal-to-noise ratios for several regions of interest, using appropriately chosen optics states. The values in Table II are for a 1 keV beam with a 1° width. The beam current has been limited to keep the instantaneous count rates (per anode) below approximately 10^5 counts s^{-1}. The signal-to-noise ratios are based upon counts when the beam is gated on and accumulated over a period of 2 ms. With the 50% duty cycle of the beam, average signal-to-noise ratios are a factor of $\sqrt{2}$ lower. Because x, the distance between the beam focus and the detector, depends upon the relative geometry of the guns, detectors, and drift step, we have taken x to be equal to the larger of either the drift step or 2 m. We have also ignored the beam spreading parallel to the magnetic field that occurs between the focus and the detector, since the sign of this extra term depends upon the specific geometry.

3.6. Requirements for Gun/Detector Configuration

In order to accommodate the time-of-flight measurements, there must be two guns, each steerable over a solid angle of 2π steradian, but facing opposite hemispheres. As the detectors require active steering into the appropriate directions, two such detectors are needed, each able to cover 2π sr. The time-of-flight technique puts no restriction on the relative location of guns and detectors (other than those imposed by field-of-view considerations).

The triangulation technique, on the other hand, requires that guns and detectors are well separated in order to provide adequate baselines. Ideally, they should not be coplanar, but rather form a tetrahedron. Otherwise there will be situations where the baseline vanishes, i.e., when **B** and $\mathbf{v}_D$ are in the gun/detector plane. As technical constraints rule out such a tetrahedron solution on Cluster, one gun and one detector are combined into a single package, and two such packages are mounted on opposite sides of the spacecraft (see Figure 3). So they are not

only coplanar, but even colinear. As a consequence, the triangulation baseline will vanish each time the projection of the two packages in the plane perpendicular to $\mathbf{B}$ is aligned with $\mathbf{v}_D$. Even though this will cause a spin-modulation of the accuracy with which the drift step is triangulated, the electron guns will stay on track. Furthermore, the time-of-flight technique, which will always be executed simultaneously with the triangulations, will not be affected at all. (Note that in the worst case of a spin axis perpendicular to both $\mathbf{B}$ and $\mathbf{v}_D$, the baseline is always zero.)

3.7. Beam Recognition, Tracking, and Coding

The electron drift technique described in the previous sections requires first a scheme capable of initially finding the beam for arbitrary directions of magnetic and electric fields; secondly, a scheme to keep the beam on target, and, finally, a scheme which determines the time-of-flight of the electrons for each beam.

As described in more detail in Section 6.1, several different schemes are implemented. The simplest of those just sweeps the beam in the plane perpendicular to $\mathbf{B}$, where the latter condition is taken from the magnetometer data received in real-time. From the continuously recorded (and transmitted) counts one can then derive the directions to the target and infer the drift velocity.

As our main operating mode, we have implemented a tracking mode where the beam is rapidly swept back and forth across S. We use correlators to distinguish beam from background electrons, and thus to recognize beam passage over the detector. We will again utilize the on-board magnetometer data to define the scan plane, i.e., the plane perpendicular to the magnetic field.

To obtain the time of flight of the electrons, the beams will be modulated with a coded waveform. By correlating the received signal with the original code, the time delay between emission and reception is measured.

3.8. Capabilities and Limitations of the Technique

The electron drift technique is capable of providing several unique measurements. First, it provides the electric field perpendicular to the magnetic field $\mathbf{E}_\perp$, including its component along the spacecraft spin axis. By contrast, the double-probe technique measures $\mathbf{E}_\perp$ in the plane of the wire booms only. Second, the electron drift technique provides the unique capability of measuring local magnetic field gradients, $\nabla_\perp B$. Third, through its time-of-flight measurements the technique also yields accurate measurements of the magnetic field strength, B. Finally, the measurements are essentially unaffected by the presence of the spacecraft. A time resolution of between 10 and 100 measurements per second is possible depending on the detector signal-to-noise ratio.

On the other hand, the electron drift technique is adversely affected by intrinsic beam instabilities, strong scattering of the beam by ambient fluctuations, large-

amplitude 'spikes' in the electric field, and very rapid magnetic field variations. All these effects can cause a loss of beam track and thus a momentary loss of data.

Furthermore, there can be signal-to-noise problems as a result of insufficient beam current and/or excessive fluxes of ambient electrons. Finally, accurate separation between electric and magnetic drifts will not always be possible when the range of beam energies is restricted to between 0.5 and 1.0 keV.

3.9. SPACECRAFT POTENTIAL

The spacecraft is normally at a potential, Φ, that differs slightly from the ambient plasma potential. As the test electrons traverse the sheath surrounding the spacecraft, they are deflected and consequently enter the region of undisturbed ambient electric field with perturbed initial conditions. Normally, this will lead to an additional displacement of the returning beam. Since the proposed measurement of $\mathbf{E}_\perp$ is based on measurements of the direction of the outgoing beam, we best express the perturbation caused by spacecraft fields in terms of the angular deflection of the outgoing beam, β. Upon return the beam may suffer a similar deflection. It is easy to estimate an upper limit of β, not taking into account the peculiarities of the field geometry:

$$\beta < e\Phi/4W \ . \tag{19}$$

In sunlight Φ is of the order of a few tens of volts. With $W = 1$ keV for the electron beam, the error introduced by this effect is comparable to the pointing accuracy of the beam.

The ASPOC instrument on Cluster is designed to keep the spacecraft potential at low values in the outer regions of the magnetosphere and in the solar wind where normal spacecraft potentials may be several volts positive. This system is based on the emission of indium ions at several keV energy and with a current of 1–10 μA. The spacecraft potential will be kept at a low positive potential relative to the ambient plasma. When the potential control system is operating, EDI can use currents up to 10^{-7} A (or possibly more) without influencing the spacecraft potential in any significant way.

Riedler *et al.* (1996, this issue) have estimated the Cluster spacecraft potential both with and without the operation of the Active Spacecraft Potential Control (ASPOC) ion emitter. They show that it takes as least 10 μA emitted ion current to reduce the spacecraft potential to under 10 V over most of the range of expected environmental plasma conditions, as characterized by $N_e\sqrt{kT_e}$. Since the maximum EDI electron current is expected to be 1 μA and the typical current to be on the order of or less than 100 nA, it can be seen that the effect on the spacecraft potential will be essentially negligible when ASPOC is operating with an ion current equal to or greater than 10 μA. We note that there is considerable uncertainty in the ASPOC calculations because of the unknown effective collection area for plasma electrons

and the unknown projected area for photoemission. There is also uncertainty in the photoelectron spectrum as the ASPOC authors have noted.

There could be a significant effect of the EDI electron beam current on the spacecraft potential when ASPOC is not operating. The electron beam can be considered to be another 'photoemission' component at an energy of 1 keV. It can be seen from the three curves in Figure 1 of Riedler *et al.* (1996); that it only takes from 10 to 30 V of spacecraft potential to reduce their assumed photoemission current to about 1 μA. At higher (positive) spacecraft potentials, an EDI beam current of 1 μA could dominate over the photoemission current and drive the spacecraft potential even more positive. It is expected in such situations that a much smaller EDI current would be used.

4. Technical Description

The essential elements of the instrument are two electron guns, two detectors with their associated analog electronics, high-voltage supplies, digital controls, and correlators; and a controller unit which includes the interfaces with the spacecraft and with other instruments (cf., Figure 5). As illustrated in Figure 6, guns and detectors are combined in pairs into a single unit, referred to as the gun/detector unit (GDU). The two GDUs are mounted on opposite sides of the spacecraft. For a detailed block diagram of the GDUs, see Figure 7.

4.1. ELECTRON GUNS

In order to be able to aim the beam at the target for arbitrary magnetic and electric field directions, the electron guns must be capable of providing a beam that can be steered rapidly into any direction within more than a hemisphere. Electron energies must be variable in order to separate $\mathbf{E} \times \mathbf{B}$ and $\nabla_{\perp} B$ drifts. At the same time the energy dispersion must be small to restrict beam spreading in space and time. Beam currents must be kept sufficiently low to avoid instabilities and/or interference with other experiments on the spacecraft. To maximize the return signal in the detectors, the angular width of the beam must be kept small, but still large enough to account for uncertainties in pointing direction. Electron time-of-flight measurements require that the beam be modulated with frequencies up to 4 MHz.

A design meeting these requirements is illustrated at the top of Figure 6. To our knowledge this is the first electron gun capable of providing narrow beams in any direction within more than a hemisphere. A conventional electron source, consisting of a tungsten cathode and several electrodes (Wehnelt, Focus, and Anode) is used to produce a narrow beam at 2.7 times the required energy. The electron energy is set by the cathode potential and can be varied between 0.5 and 1.0 keV. The spread in energy is determined by the thermal spread (≈ 0.2 eV) and the variation of the potential over the emitting part of the cathode which is ≈ 0.5 eV. The beam

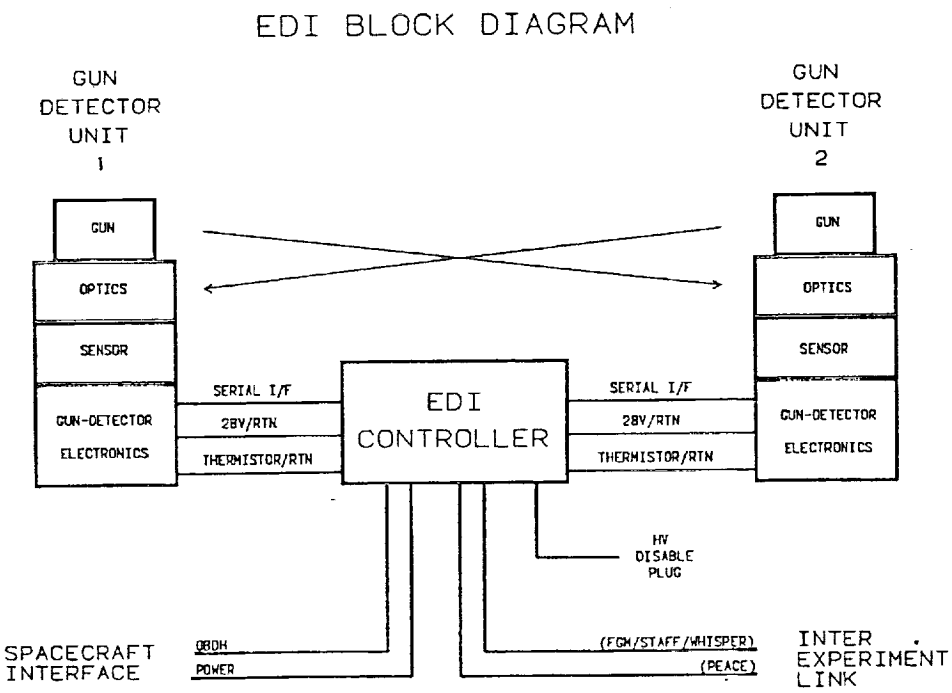

Figure 5. Overall block diagram showing the elements of the EDI instrumentation and their interrelation.

current is controlled via the current applied to the tungsten filament and can be varied between 0.1 and 2000 nA. The beam is intensity-modulated by superposing the code-signal from the correlator onto the static Wehnelt voltage via a fibre-optic cable.

After exiting from the anode, the beam is deflected into the desired azimuth direction by an octopole arrangement of electrostatic deflectors. The electrons then approach a high-transmission grid at ground potential. This retarding potential decelerates the electrons to their final energy. Since it is mainly the energy along the symmetry axis that is removed when the electrons approach the grid, the deflection angle is amplified. Figure 8 shows the voltages, equipotentials and the computed electron trajectory for the case of 90° deflection. A maximum deflection angle of more than 100° has actually been achieved. The beam width ranges from typically 1° circular for small deflection angles to 2–4° elliptical at large polar angles.

The deflection grid is made of fine copper-beryllium wires woven into a mesh that is then formed into a basket shape, welded to a steel flange, and finally gold-plated. The smaller radius of curvature used for the outer section serves to reduce shadowing by the wires by increasing the angle between beam and grid at large deflection angles. Nevertheless, the mesh introduces a 50% drop-off in beam

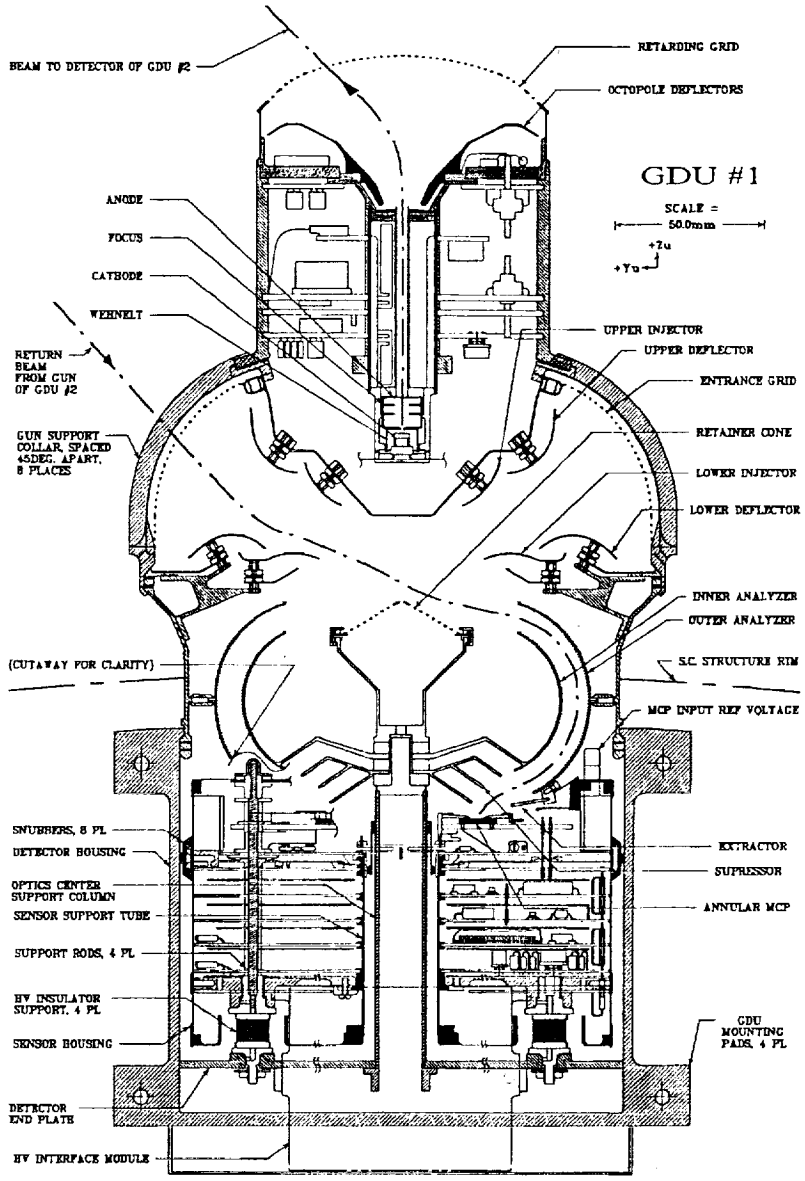

Figure 6. Cross-sectional view of a gun/detector unit (GDU). The cylindrical section at the top is the electron gun, with its filament and control electrodes at the bottom of a long drift tube from where the electrons enter the octopole deflector before they are slowed down and further deflected by the curved retarding grid. The gun is supported by a collar that bridges the detector aperture. Independently selectable voltages on 9 electrodes determine the optical properties of the detector: the polar angle of its look direction, the sensitive area for parallel beams, and the energy-geometric factor for ambient particles. An annular MCP followed by a ring of 128 discrete anodes detects the electrons at their azimuth angle of arrival. The entire sensor section rests on 4 insulator supports and floats at between +2 and +4 kV to pre-accelerate the electrons and bias the MCP. Signals to and from the sensor are routed via optocouplers. Except for 8 narrow struts in the gun-support collar, there is no obstruction of the electron trajectories. For some of the lower optics electrodes that design goal required a support column through the center of the sensor. Note that the GDE section of the unit has been omitted for clarity.

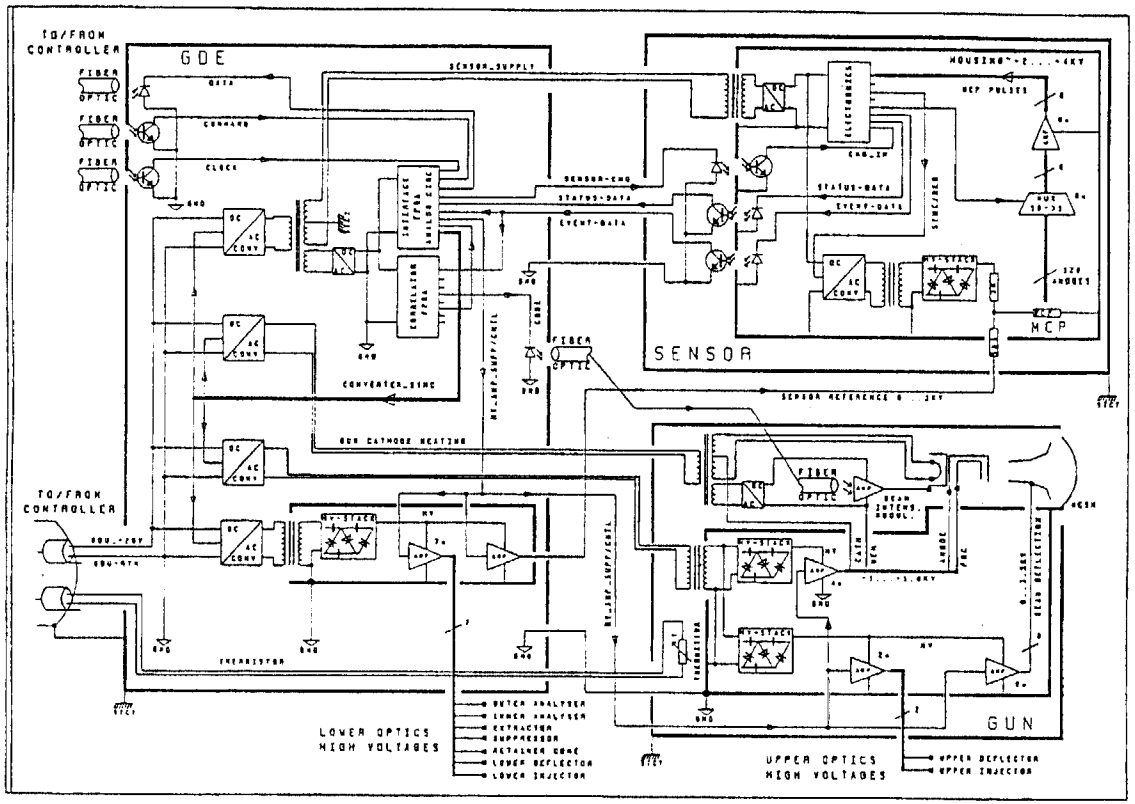

Figure 7. GDU electronics block diagram. The part on the left, designated GDE, provides the power supply for the entire GDU; the D/A and A/D conversions for the signals exchanged via a serial interface over fibre-optics cables with the controller unit; the correlators for the time-of-flight determination; and the high-voltage stack and voltage amplifiers for the lower-optics electrodes. The upper right-hand part shows the sensor section with its programmable MCP high-voltage supply, anode selection logic and the 8 pulse amplifiers/discriminators. The section at the lower right shows the electronics in the gun, with its filament current supply, and its two high-voltage stacks and associated HV amplifiers for the gun and upper optics electrodes, respectively.

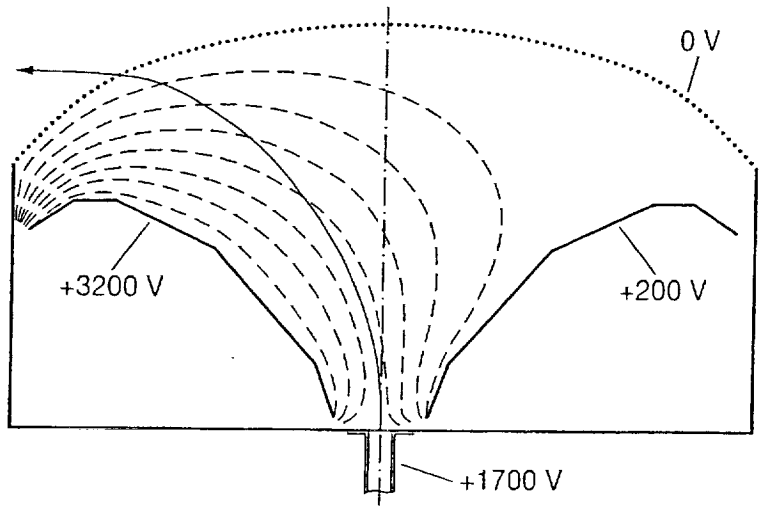

Figure 8. Illustration of the novel beam deflection scheme developed for the EDI electron guns. After exiting the anode that accelerates the 1000 eV electrons emitted by the cathode to 2700 eV, the beam is deflected in the electrostatic potential pattern (dashed lines) produced by two (of eight) deflectors and the outer curved grid (dotted line) that is at ground potential. For the 90° deflection shown the deflectors are at 200 V and 3200 V, respectively. The retarding potential on the grid slows the electrons to their final energy of 1000 eV and bends the trajectories to the desired deflection angle. By changing the voltages on the deflectors, any deflection angle between 0 and 100° can be produced. There are 8 deflectors that are arranged as an octopole to allow deflection of the electron beam at arbitrary azimuth angles. This way the beam can be steered into any direction over more than a hemisphere.

intensity at large deflection angles, as well as some structure in the beam intensity profile.

The gun voltages are generated by individual high-voltage amplifiers that use the light from LEDs to control the leakage current of two high-voltage (HV) diodes connected in a push-pull configuration between the plus- and minus-sides of a HV stack. The control voltages for the eight HV amplifiers of the octopole deflector are derived from two reference voltages, DX, DY, provided by the controller. Deflector voltages are derived from a separate stack and range up to 3.4 kV.

4.2. Detectors

The demands of the Electron Drift Instrument require a detector design that is different from anything flown before. It must be able to look in any direction within a region greater than a 2π steradian hemisphere. To compensate for the low returning beam fluxes, the detectors must have a large effective area, as much as two or three square centimeters. Unlike the natural plasma, the returning beam is monoenergetic and unidirectional. Therefore, the signal-to-noise ratio may be improved by designing the detector to be selective in velocity space. To make continuous electric-field measurements while either magnetic or electric fields

vary rapidly, the detectors must be capable of changing their look directions in less than a millisecond. As they cannot be shrouded in any direction, they must have good internal light rejection.

The detector system that we designed to meet these requirements is illustrated in Figure 6. It consists of an optics section, a programmable sensor, associated electronics, and voltage generators. Adjustment of the look direction is achieved in elevation by deflecting the incoming beam, and in azimuth by selecting a contiguous set of sectors of the annular image-region on the sensor micro-channel plate (MCP). The incoming beam of electrons is monoenergetic and monodirectional, and illuminates the entire detector. The large effective area is achieved with double focussing, as explained in Section 4.2.1. Here, 'double focussing' refers to the simultaneous concentration of the beam in two angular planes, rather than in the more commonly understood sense of energy and angle.

To cover all beam directions, two identical detectors are mounted such that they view opposite hemispheres. We have called this detector system 'Janus', after the Roman god with the two back-to-back faces.

4.2.1. *Optics*

After passing through the optics aperture screen, the beam electrons encounter a large transverse electric field generated by the two deflector electrodes on each detector. The injectors also contribute an electric field with components transverse to the particle trajectory and in the radial direction of the detector's cylindrical coordinates. As these electrodes are exposed to sunlight, they cannot be biased negatively or they would expel photoelectrons that would interfere with other spacecraft experiments. The retainer cone provides additional control of transverse and radial electric fields in the central region of the optics. Because the retainer cone at times may be biased negatively, it is constructed from a wire mesh to minimize the surface area from which photoelectrons emanate.

As illustrated in Figure 9, the electron beam is focussed in cross sections parallel to the z axis ('polar' focussing) near the entrance of the electrostatic analyzer, and again near the exit of the analyzer. In the projection perpendicular to the z axis ('azimuthal' focussing), the beam is partially focussed and then diverged before it enters the analyzer, in such a way as to exploit more effectively the final azimuthal focussing that occurs within the analyzer. Together, the deflectors, injectors and retainer cone constitute an 'immersion lens' that projects the beam past the central region into the entrance of the electrostatic analyzer, thereby increasing the effective area of the aperture. The azimuthal focussing also extends the width of the effective aperture area and thus reduces the effects of shadowing caused by the gun-support struts shown in Figure 6.

The deflector potentials play the most important role in determining the polar look direction; the injector potentials are varied primarily to maintain azimuthal beam spread at large deflection angles, but they also influence the look direction;

and the retainer-cone potential provides additional control over the azimuthal focus and polar look direction.

The inner- and outer-analyzer electrodes select electrons in the desired energy range, and their toroidal shapes also contribute to azimuthal focus, as seen in Figure 9. Emerging from the electrostatic analyzer, the electrons pass between two additional electrodes: the extractor and the suppressor. These electrodes adjust the radial position of the MCP image and direct the electrons to strike the MCP with impact angles closer to the surface normal.

Nine independently programmable high-voltage supplies are needed to operate the optics subsystem. A tenth programmable supply sets the sensor-reference voltage. For electron drift measurements, all voltage except the sensor reference are scaled with energy; the voltage on the latter is kept fixed because its capacitative time constant does not permit rapid changes. Although all ten electrode voltages can depend on polar angle, in order to conserve controller resources we vary only the five that depend most strongly on polar angle (deflectors, injectors and retainer cone). All voltages are generated by the same type of HV supplies already referred to in the Gun section.

For a given beam energy and polar angle, different combinations of these voltages can be chosen to obtain different collection areas, A, for the beam and different geometrical factors, H, for the ambient ('background') electrons (cf., Table II). Therefore, with appropriate combinations of voltages we can optimize beam-signal levels or signal-to-noise (SNR) levels, depending on the circumstances. Also, combinations of these ten voltages can be chosen to achieve other special optical characteristics, such as wide or narrow values of polar-angle acceptance or energy bandpass. For example, the detector's energy bandpass can be adjusted for a given incident particle energy by setting independently the voltage difference between the plates (to control the actual bandpass width) and the average voltage on the analyzer plates (to shift the energies of the particles of interest to lie inside the passband as they enter the analyzer). In addition, combinations of voltages can be chosen that achieve almost all of the above characteristics, but measure ions instead of electrons. Figure 10 illustrates sample ion trajectories at a specific energy and initial direction.

To simplify matters, we use a finite number of such voltage combinations, called optics 'states'. Table III lists the beam collection areas A, geometric factors H and acceptance angles for the 'states' presently intended for the electron drift measurements. For each state there is a look-up table from which the voltages that vary as a function of the polar angle are obtained. State 6 has the largest sensitivity A for beams, but also a large H-factor for ambient electrons, and thus not a good SNR. State 3 has the highest SNR, but less than half the area of State 6. States 2 and 7 have only modest SNR, but large acceptance angles, and thus are suited for cases where there is uncertainty in δ, the angle change of the returning beam. State 4, finally, is a 'shut-down' state, to be used when fluxes are very high.

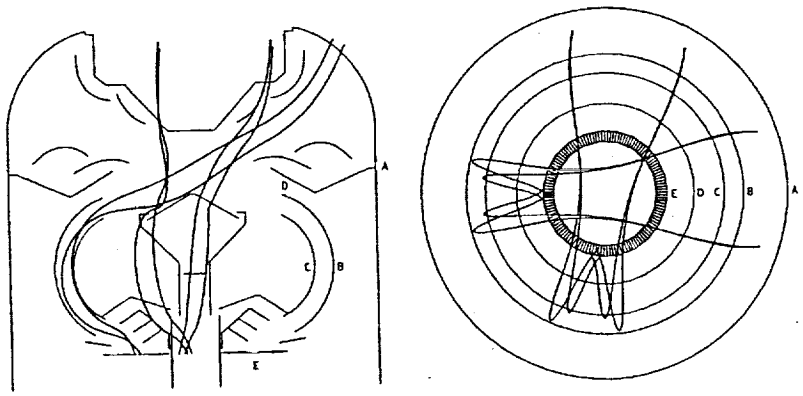

Figure 9. Computer-generated sample trajectories of 1 keV monodirectional electrons at a polar angle of 27°, projected in the (x, z) and (x, y) planes respectively. Two families of four trajectories are shown; these families are identical except for an azimuthal rotation of 80°. Note the two focal points in the (x, z) projection, near the entrance and exit of the analyzer respectively. In the (x, y) projection, note the convergence and divergence of the beam as it traverses the central region of the optics prior to entering the analyzer, followed by the strong azimuthal focussing within the analyzer. The (x, y) projection displays the following selected parts and boundaries of the detector: (A) outer radius of aperture grid; (B) outermost radial extent of outer analyzer plate; (C) outermost radial extent of inner analyzer plate; (D) radial edge of outer analyzer at entrance; (E) sensor annulus.

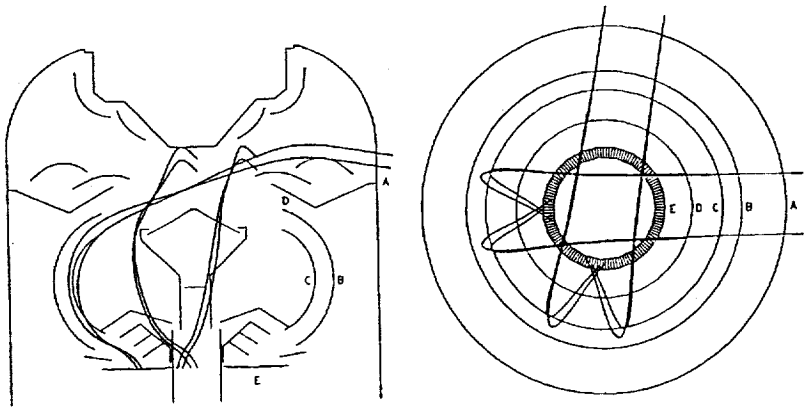

Figure 10. Sample trajectories of 1 keV monodirectional protons at a polar angle of 100°, projected in the (x, z) and (x, y) planes respectively. Two families of four trajectories are shown; these families are identical up to an azimuthal rotation of 80°. Note that focussing in the (x, z) projection occurs twice, as it does for electrons, although not in the same locations as for electrons. In the (x, z) projection, the azimuthal focussing in the central region is more subtle than for electron cases, but the contribution of the analyzers to azimuthal focussing is again clearly evident. The (x, y) projection displays selected parts and boundaries of the detector (see caption to Figure 9).

4.2.2. *Sensor*

Electrons are imaged by the detector optics within the selected polar angle acceptance cone, onto an annular microchannel plate (MCP) stack that is the input to the sensor. Except when the direction of the returning beam is close to the z axis,

Table III
Optics states

State	A	H	Angle
2	2.2	0.110	20
3	2.7	0.016	7
4	0.5	0.001	4
6	5.8	0.210	10
7	1.3	0.022	14

A is the collection area (cm^2) for beams.
$H = G(\Delta E/E)$ is the geometric factor (cm^2 sr eV/eV) for ambient electrons.
Angle is the FWHM acceptance angle (deg).

only a limited azimuthal segment of the image annulus is illuminated by beam electrons, whereas the entire annulus collects ambient electrons that are incident within the optics acceptance cone and energy passband. Under command of the controller, the sensor responds only to events within a selected azimuthal range, thus complementing the polar angle selection that is performed by the optics.

The sensor collects the amplified electron events, which are produced by the MCP stack operated in the pulse-counting mode, on an annular array of 128 discrete anodes. Signals from each anode are routed to one of eight custom hybrid multiplexers, each with 16 single-anode inputs, and whose outputs are routed, in turn, to eight high speed programmable-threshold preamplifier/discriminator hybrids. The sensor control structure is designed so that any eight contiguous anodes in the annular array (22.5° of azimuth) may be selected as the instantaneous field of view. A second-level multiplexer, implemented within an ACTEL programmable gate array, further selects the discriminator outputs to provide two digital output channels. The anodes routed to these two outputs are selected by two arbitrary and independent 'pointer field' bit masks within the eight-anode field of view. Typically, one of the output channels is routed to the instrument correlator for recognition of the electron beam, while the other is available for accumulating total counts or monitoring background.

The electrical potential of the sensor input MCP is established by the detector optical requirements. The sensor internal electronics and housing float at typically +2 kV above this input potential due to the internally generated HV bias voltage across the MCP stack. Sensor power, signal pulses, commands and status are coupled to the rest of the GDU electronics via a high voltage isolation module containing an isolation transformer and 9 fiber optics signal links.

4.3. Correlators

To detect the beam electrons in the presence of background counts from ambient electrons and to measure their flight time, the electron beam is intensity-modulated

with a pseudo-noise code (PNC). The modulation is achieved by changing the Wehnelt control voltage such that the beam is successively turned on and off. In order to reject detector signals from the gun in the same unit, the codes for the two gun-detector pairs are inverted relative to each other. The modulation frequency can be chosen between 8 kHz and 4 MHz in order to cover the range of expected time delays and to obtain adequate delay-time accuracy.

The stream of electron event pulses received by the detectors are fed in parallel into an array of counters, each one gated with its individual copy of the PNC, shifted by one chip from counter to counter, and delayed as a whole (by a variable amount) against the PNC used to modulate the outgoing beam. The counter that is gated with a PNC matching the flight time will receive all the beam event ('signal') plus half the background events, while all others receive only half the signal plus half the background. A drift and tracking control loop ('auto-track') varies the delay of the correlator codes relative to the gun code such that the signal is kept in one dedicated counter while the flight time changes as a result of changing magnetic and electric fields.

We first experimented with a long (4095-chip) code. Codes whose lengths exceeds the electron flight time have the advantage that the times can be determined without ambiguity. But since one can only realize a finite number of correlator channels, one must have a very good estimate of the time of flight to properly delay these channels (e.g., to within 0.3% for 15 channels and 4095 chips). Even if the gyro time were known precisely from the on-board magnetometer data, the unknown electric field can cause variations of up to 10%. Thus one would have to vary the code-delay until the time of flight is within the range covered by the 15 correlators.

Because of these problems with long codes, we have finally implemented a short (15-chip) code and 15 correlator channels. Such a solution has the advantage that beam electrons are always counted in one of the channels, regardless of flight time. On the other hand there is the disadvantage that the flight time is determined only modulo the code duration. This ambiguity can usually be removed by starting out with a sufficiently low code-clock frequency such that the entire range of expected flight times fits within one code-length. This initial choice of frequency is based on the gyrofrequency computed from the magnetometer data and an assumed 10% variation in flight-time to account for large electric fields.

The correlator electronics resides in a RAM-based Field-Programmable Gate Array (FPGA) of the XILINX type. Configuration of the FPGA is part of the start-up procedure of the instrument. As the configuration file is held in EEPROM (electrically erasable PROM), other correlator schemes could be uploaded in flight if necessary.

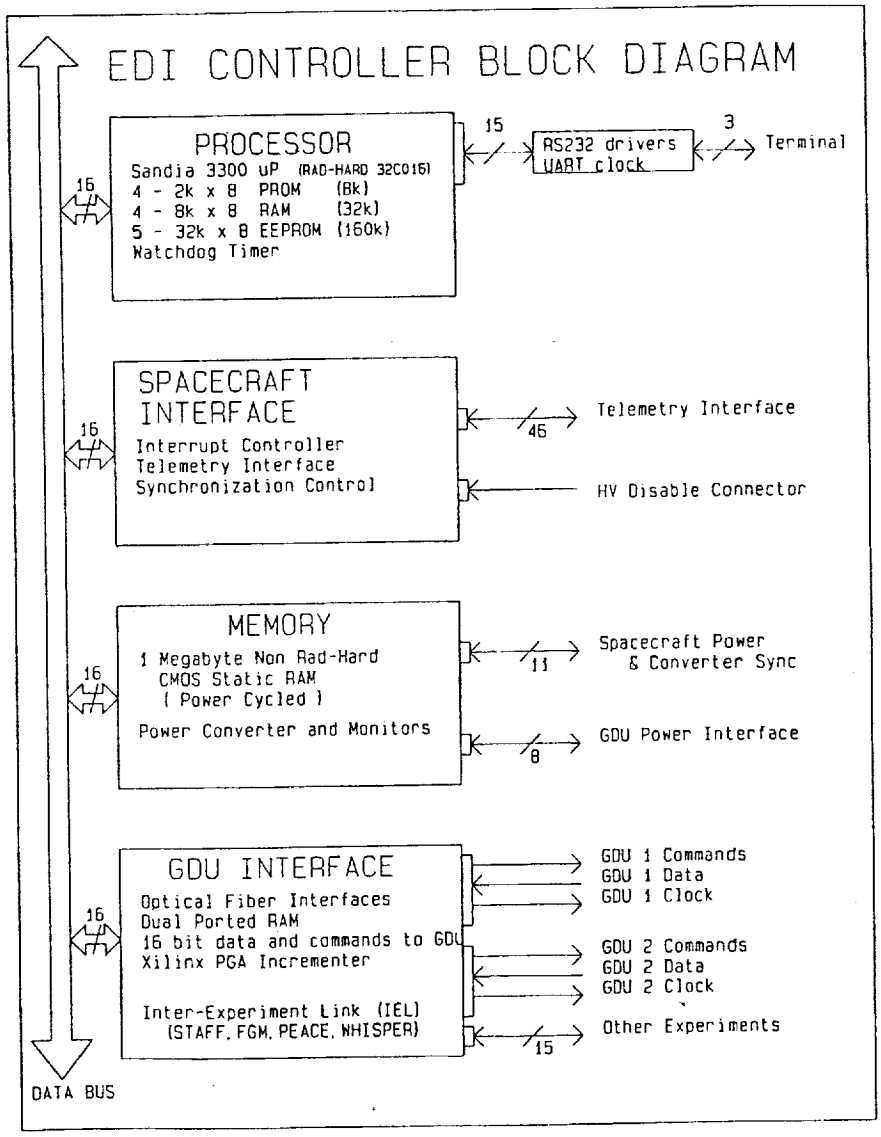

Figure 11. Controller functions.

4.4. CONTROLLER

Based upon information from the detectors and the magnetometers, the controller programs the guns and detectors. It establishes beam coding and tracking patterns and handles all interfaces with the spacecraft and with other instruments. This central processor also transfers the programmed gun firing directions (for beams returning to the detectors), plus the timing information from the correlators, to the

necessary telemetry data so that the resultant drift-step direction and magnitude can be determined on the ground.

Figure 11 is a sketch of the configuration of the controller. We use a Sandia 3300, a radiation-hardened version of the NSC 32C016, as our central processor. The associated memory has 8 kB of fuse-linked PROM, 160 kB of EEPROM, and 32 kB of static RAM. The fuse-linked PROM contains the software for system initialization, housekeeping, and basic telemetry routines. The EEPROM, which is reprogrammable via spacecraft commands, contains three types of information. Science data algorithms and higher-level telemetry handling make up 48 of the 160 kB of EEPROM. 80 kB are reserved for gun and optics voltage tables. 32 kB are reserved for FPGA configuration data. The 32 kB of CMOS static RAM is available for local storage of various parameters and variables, and also serves as telemetry-data buffer. The controller includes 1 MB of non-hardened memory for storage of burst mode or diagnostic data. This memory can store approximately seven seconds of data recorded at the highest possible time resolution, or approximately one minute of data recorded at debugging speeds.

The controller communicates with the spacecraft, with other instruments, and with the gun/detector electronics. The spacecraft interface handles all science and housekeeping telemetry as well as inputs such as time-tagging and commanding. Inter-experiment links include magnetic field information from FGM and STAFF, a blanking pulse from WHISPER to warn of possible interference from that active experiment, and a blanking pulse sent from EDI to PEACE when the EDI electron beam could interfere with the PEACE electron measurement. This interface with the GDUs is controlled by an FPGA contained in the controller and sends commands from the controller to the GDUs that change the gun and detector hardware parameters, and receives data back from the GDUs, including detector count rates, correlator information, and housekeeping data. The physical interface consists of three optical-fiber cables for each GDU, carrying serial information.

The fundamental functional time step of the EDI instrument is the controller's basis cycle interrupt (BCI), which is nominally 2 or 4 ms. Every BCI, the controller will use the information it receives from the various interfaces to calculate new parameters for directing the beams and the detectors. In the tracking modes of operation, the time step is 4 ms. Tracking tasks that operate on longer time scales, such as slowly changing the beam current or modifying the detector's basic optics state, are driven by a priority-queue that is controlled by a task manager. A 10 ms interrupt or an asynchronous service call initiates the task manager.

4.5. Resources

The GDU mass is 4550 g each and that of the Controller 1610 g. The total power consumption is 9.5 W. The science data rates allocated to EDI are 1520 bit s^{-1} in normal-mode telemetry, and 10780 bit s^{-1} in burst-mode telemetry. An additional 140 bit s^{-1} are used for housekeeping data.

5. Calibrations and Simulations

The electron guns were calibrated at MPE in a dedicated facility at electron energies of 0.5 and 1.0 keV up to the maximum deflection angle of 104°, and over the entire 360° in azimuth, with a grid size of 4° and an accuracy of approximately 0.5°. Information on beam profiles and beam intensity control were also gathered during this process.

The EDI detector is calibrated with both a laboratory system and a computer model. The laboratory system simulates the diverged returning EDI beam with an electron gun and two parallel-plate beam mirrors; by manipulating the voltages within these mirrors, the beam can be made to 'raster' across the detector aperture as counts are accumulated on the detector's image plane. Thus a parallel family of narrow beams is used to simulate a broad monodirectional beam. Background is simulated by scattering a second beam from a target. By measuring 'foreground' sensitivity of the optics to the rastered beam and 'background' sensitivity of the optics to the scattered beam, and supplying these quantities to an optimization algorithm that controls the optics voltages, we can determine voltage combinations that achieve desirable optical properties such as high sensitivity and high signal-to-noise ratio, at selected polar angles. A set of such voltage combinations covering all polar angles of interest comprises a 'state'. Adequate rotational symmetry of the optics was verified with a special test setup during EDI acceptance testing.

The computer model of the optics can simulate and display particle trajectories through the detector optics, and accumulate macroparticle 'counts' into bins on the image plane. The user may select sequences of initial conditions for these trajectories so as to cover the regions of phase space to which the detector is sensitive, and thereby determine effective aperture areas, geometrical factors, sensitivity profiles as a function of polar angle, and related quantities. Also, by following a cycle of changing the voltages on the optics electrodes and observing the changes in the displayed particle trajectories, one may evaluate voltage combinations as candidates for inclusion in an optics state.

Because of the large scale of the electron gyroradius and gyroperiods for which the EDI is designed, it is not possible to perform ground tests that fully exercise the instrument. In order to validate its closed loop operation and demonstrate the function of the control algorithms, we have built a tracking simulator that closes the loop between gun and detector even though no beam is actually generated and no electrons detected. The simulator contains a set of tabulated values that are obtained by calculating the proper beam-firing directions and detector-look directions for simulated magnetic and electric fields that are based on actual data measured with instruments on AMPTE-IRM. It feeds these same magnetometer data to the controller via the interface that is used in flight to receive data from the FGM instrument, and taps into the serial interface between controller and GDUs. It compares, against the tabulated values, the instructions which the controller issues to the gun and detector. From the match or mismatch of beam firing directions (the

ntroller-generated instructions vs. the tabulated proper directions), the tracking mulator computes how much, if any, flux arrives at the detector. It adds simulated uxes of ambient electrons that are also based on AMPTE-IRM measurements. rom the detector settings chosen by the controller, the tracking simulator computes ie count rates which would result in the sensor, separately for beam and ambient ectron fluxes.

Two modes of operation are then possible. Either the count rate information directly provided to the controller via the serial interface, in which case the orrelator characteristics have to be simulated as well; or the simulator directs edicated hardware pulsers to generate streams of beam and background pulses. he beam pulse stream is modulated with a properly delayed copy of the pseudo-oise code of the outgoing beam in order to reflect the electron time of flight. This vay the hardware implementation of the correlators is truly tested instead of being imulated.

The controller tracking software uses these count-rate results, as well as the nagnetic-field data it is receiving, as the basis for deciding on the instructions t will send out to the GDUs in the next time step. Running through different imulated data files, we can test and optimize the software and its underlying lecision algorithms for their ability to cope with realistic magnetic and electric ields, as well as the implied flux levels and signal-to-noise ratios.

6. Science Modes and Telemetry Data

6.1. ELECTRON DRIFT MEASUREMENTS

The simplest operational mode is modelled after the original GEOS application. In this mode, the two beams are steered into directions which are anti-parallel to each other and transverse to the magnetic field. The latter condition will be computed from the magnetometer data received in real-time. Rotation of the satellite will first cause beam 1 and then beam 2 to hit the target S and strike the detectors. Telemetered data consist of a time-series of detector counts from which two drift velocities per satellite rotation can be reconstructed on the ground.

A simple variant of the GEOS Mode, referred to as Rapid Spin (RS), sweeps the beam in the plane perpendicular to **B** at a selectable rate up to 1° per ms. This is a considerable improvement in speed over the GEOS mode where the angular sweep rate is fixed by the satellite rotation, i.e., 0.09° per ms.

Neither GEOS nor RS modes track the target. Our basic tracking mode, referred to as Windshield-Wiper (WW) Mode, uses the RS mode until each beam has hit its target, $S1$ and $S2$. Once this has occurred, we will continuously track $S1$ and $S2$ independently, by sweeping the beams rapidly back and forth across them, in the plane perpendicular to **B**. This is a great improvement over the GEOS and RS schemes, in which the beam is fired at S only when either the spacecraft rotation or

the passive angular sweep is at the correct phase. In the 'windshield-wiper' scheme, which is illustrated in Figure 12, the firing direction is controlled actively by the instrument so that the beam hits (or is very near) S all the time.

To recognize that the beam is returning to the detector, the controller constantly (once every 2 ms) computes the signal-to-noise ratio from the maximum and minimum counts in the set of correlator channels. If that ratio exceeds some (selectable) limit, it is assumed that the beam is striking the detector. Initially we will steer each detector to look at a direction anti-parallel to the emission direction of the associated beam. This works as long as the aberration angle δ introduced above is less than the acceptance angle of the detector. For larger aberration angles the detector look-direction must be offset appropriately. This complicates target acquisition.

The 'windshield-wiper' software, which keeps the target direction tracked in angle space, is interwoven intricately with the time-tracking software, which keeps the time-of-flight information available. As noted earlier, the beams are modulated with a coded waveform. Correlating the received signal, after a delay corresponding to the time of flight, with the original coded signal, has two important functions. First, correlating the return signal with the fired signal allows a significant increase in signal-to-noise ratio. Second, the delay that results in the largest correlated signal corresponds to the time of flight of the electron beam.

In the WW-mode, telemetered data consist of the firing angles when the two beams were on target, and the two associated electron times-of-flight, plus timing and quality information. With the allocated telemetry rate it is possible to transmit this set of measurements every 64 ms in nominal-mode (NM) telemetry and every 16 ms in burst-mode (BM1) telemetry. From the telemetered data one can then derive the drift velocities and the magnetic field strength, in BM1 telemetry and under ideal tracking conditions as often as every 16 ms.

We are also working on a '2D-Tracking' Mode in which, after the target has been acquired, the beam is steered according to target-direction estimates based upon Kalman filtering of the observed signals.

6.2. AMBIENT PARTICLE MEASUREMENTS

The EDI detectors are capable of measuring both electron and ion particle distributions. Each of the two detectors can be commanded to look in any direction over greater than a 2π steradian hemisphere, and since the two detectors are mounted on opposite sides of the spacecraft with their symmetry axes pointing in opposite directions, full-sky surveys can be achieved without relying on spacecraft spin to complete the coverage of phase space. In addition, since the $\mathbf{B}$ field is known to the EDI controller via the on-board magnetometer data, specialized surveys can be performed in coordinates fixed with $\mathbf{B}$, and they can be performed continuously.

The ambient mode that exploits this ability to scan selectively in coordinates fixed with $\mathbf{B}$ is the Pitch Angle Surveys and Ion Flows (PASIF) mode. This mode contains three sub-modes: (1) pitch-angle surveys, (2) perpendicular ion flows, and

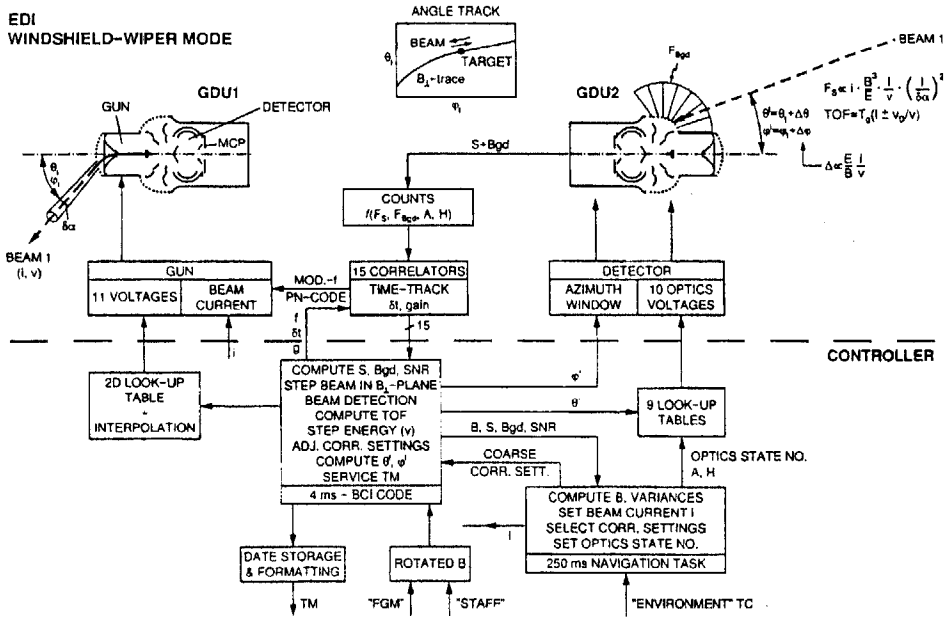

Figure 12. Illustration of the Windshield-Wiper mode of operation. The electron beam from GDU1, characterized by its current i, speed v, direction Θ and ϕ, width $\delta\alpha$, modulation frequency f and code-type, is swept in the plane perpendicular to **B**, as determined from the FGM and STAFF magnetometers. Signals recorded by the detector in GDU2 are analyzed to determine when the beam is on target. A similar link (not shown) exists between the gun in GDU2 and the detector in GDU1. The detector count rate consists of the background signal (Bgd) from the flux of ambient plasma electrons (F_{Bgd}) and the beam signal (S) from the incident flux of beam electrons (F_S) if the beam is on target. Correlators are used to distinguish beam and background electrons, as well as to measure the time-of-flight of the beam electrons. Once beam passage has occurred, the sweep direction of the beam is reversed and the process repeated, as indicated in the box at the top of the figure. For small E/B, the return beam is directed parallel to the emitted beam, but for large E/B there is a significant offset, Δ. Every 4 ms the controller exercises a software loop that directs beams and detectors, and sets the correlator parameters. A navigation task running every 250 ms selects beam currents, optics states, etc. Look-up tables are used to convert directions into deflection voltages.

(3) parallel ion flows. The pitch-angle sub-mode allows pitch-angle distributions to be measured for either electrons or ions at a sequence of directions spaced equally in pitch angle, starting with the $+\mathbf{B}$ and $-\mathbf{B}$ directions for each detector respectively. The number of pitch-angle directions and spacing between directions can be changed via mode initialization tables.

The perpendicular-ion sub-mode of PASIF permits surveys in the plane perpendicular to $\mathbf{B}$ at equally-spaced azimuthal directions. This sub-mode will be used with azimuthal spacings at or near 30° and 60° and can be used to infer ion flow velocities perpendicular to $\mathbf{B}$.

The parallel-ion sub-mode of PASIF permits surveys in a family of cones with the $\mathbf{B}$-field direction as their common axis. Such surveys will reveal the angular offset from the $\mathbf{B}$ direction of the distribution peak in the nearly field-aligned flows, thereby allowing for cases with perpendicular ion flows.

The maximum and minimum voltage limits available to the EDI optics were chosen originally to allow electron beams of energy 1 keV or less to be detected over all desired look directions in a region greater than a 2π steradian hemisphere. As we scale the optics voltages to observe ambient particles of energy greater than 1 keV, we may reach these limits on some electrodes, particularly the deflectors. This will cause the look directions at some extreme polar angles (near the pole and the equator) to become inaccessible at higher energies. Also, because the ion states achieve different polar look-angles by repulsively reflecting the ions entering the aperture grid, the sensitivity of the optics to ions decreases in the neighborhood of the pole and vanishes at the pole. In the relatively extreme case of observing ions at 10 keV, polar angles between 48° and 90° can still be achieved, providing access to two thirds of a hemisphere.

Acknowledgements

We acknowledge the contributions to the EDI proposal of the co-investigators A. Pedersen (ESA/ESTEC), V. Formisano and E. Amata (CNR), K. Tsuruda, M. Nakamura and H. Hayakawa (ISAS). We are indebted to the following individuals for the part they have played in instrument manufacture, testing and qualification: at MPE, P. Obermayer, K.-H. Kaiser, E. Künneth, W. Goebel, W. Stöberl, K. Sigritz, and the staff of the workshops headed by G. Pfaller, P. Reiss, and L. Pichl; at UCSD, G. Kendrick, J. Ritter, S. Beros, and K. Larson; at UNH, J. Googins, C. Kletzing, K. Mello, S. Turco, P. Kelly, W. Isaac, D. Hallmark, D. Bodet, and P. Vachon; and at LPARL, M. Gabriel, G. King, K. Strickler, and E. McFeaters.

References

Aggson, T. L. and Heppner, J. P.: 1977, 'Observations of Large Transient Magnetospheric Electric Fields', *J. Geophys. Res.* **82**, 5155.

Baumjohann, W. and Haerendel, G.: 1985, 'Magnetospheric Convection Observed Between 06:00 and 21:00 LT: Solar Wind and IMF Dependence', *J. Geophys. Res.* **90**, 6370.

Baumjohann, W., Haerendel, G., and Melzner, F.: 1985, 'Magnetospheric convection observed between 06:00 and 21:00 LT: Variations with Kp', *J. Geophys. Res.* **90**, 393.

Baumjohann, W., Sckopke, N., LaBelle, J. K., Klecker, B., Lühr, H., and Glassmeier, K. H.: 1987, 'Plasma and Field Observations of a Compressional Pc 5 Wave Event', *J. Geophys. Res.* **92**, 12203.

Cowley, S. W. H.: 1978, 'A Note on the Motion of Charged Particles in One Dimensional Magnetic Current Sheets', *Planetary Space Sci.* **26**, 539.

DeForest, S. E. and McIlwain, C. E.: 1971, 'Plasma Clouds in the Magnetosphere', *J. Geophys. Res.* **76**, 3587.

Escoubet, P., Schmidt, R., and Goldstein, M. L.: 1996, 'Cluster: Science and Mission Overview', *Space Sci. Rev.* , this issue.

Hones, E. W., Jr.: 1979, 'Transient Phenomena in the Magnetotail and Their Relation to Substorms', *Space Sci. Rev.* **23**, 393.

McIlwain, C. E.: 1972, in B. M. McCormac (ed.),*Earth's Magnetospheric Processes*, D. Reidel Publ. Co., Dordrecht, Holland, p. 268.

McIlwain, C. E.: 1981, in S.-I. Akasofu and J. R. Kan (eds.),*Physics of Auroral Arc Formation*, AGU, Washington, p. 173.

Melzner, F., Metzner, G., and Antrack, D.: 1978, 'The GEOS Electron Beam Experiment', *Space Sci. Rev.* **4**, 45.

Paschmann, G., Melzner, M., Haerendel, G., Bauer, O. H., Baumjohann, W., Sckopke, N., Treumann, R., McIlwain, C. E., Fillius, W., Whipple, E. C., Torbert, R. B., and Quinn, J. M.: 1993, in W. R. Burke (ed.),*Cluster: Mission, Payload and Supporting Activities*, ESA SP-1159, p. 115.

Pedersen, A., Grard, R., Knott, K., Jones, D., Gonfalone, A., and Fahleson, U.: 1978, 'Measurements of Quasi-Static Electric Fields Between 3 and 7 RE on GEOS-1', *J. Geophys. Res.* **22**, 333.

Pedersen, A., Cattell, C. A., Fälthammar, C.-G., Formisano, V., Lindqvist, P.-A., Manka, R. H., Mozer, F. S., and Torbert, R.: 1984, 'Quasistatic Electric Field Measurements with Spherical Double Probes on the GEOS and ISEE Satellites', *Space Sci. Rev.* **37**, 269.

Riedler, W., Torkar, K., Rüdenauer, F. *et al.*: 1996, 'Active Spacecraft Potential Control', *Space Sci. Rev.* , this issue.

Sheldon, R. B. and Gaffey Jr., J. D.: 1993, 'Particle Tracing in the Magnetosphere: New Algorithms and Results', *Geophys. Res. Letters* **20**, 767.

Sheldon, R. B. and Hamilton, D. C.: 1994, 'Ion Transport and Loss in the Earth's Quiet Ring Current: 2. Diffusion and Magnetosphere Ionosphere Coupling', *J. Geophys. Res.* **99**, 5705.

Tsuruda, K., Hayakawa, H., and Nakamura, M.: 1985, in A. Nishida (ed.),*Science Objectives of the Geotail Mission*, ISAS, Tokyo, p. 234.

The Electron Drift Technique for Measuring Electric and Magnetic Fields

G. Paschmann[1], C. E. McIlwain[2], J. M. Quinn[3,4], R. B. Torbert[4], and E. C. Whipple[5]

The electron drift technique is based on sensing the drift of a weak beam of test electrons that is caused by electric fields and/or gradients in the magnetic field. These quantities can, by use of different electron energies, in principle be determined separately. Depending on the ratio of drift speed to magnetic field strength, the drift velocity can be determined either from the two emission directions that cause the electrons to gyrate back to detectors placed some distance from the emitting guns, or from measurements of the time of flight of the electrons. As a by-product of the time-of-flight measurements, the magnetic field strength is also determined. The paper describes strengths and weaknesses of the method as well as technical constraints.

1. INTRODUCTION

The electric field is an essential quantity in space plasmas, yet it is one of the most difficult to measure. This is because in many important circumstances the electric fields are very small (less than 1 mV/m) and the plasma is very dilute. Under such circumstances it is often difficult for the conventional double-probe technique to distinguish natural fields from those induced by spacecraft wakes, photoelectrons, and sheaths. The electron drift technique has been developed to check and complement the double-probe technique. The drift method involves sensing the drift of a weak beam of test electrons emitted from small guns mounted on the spacecraft. This drift is related to the electric field, but gradients in the magnetic field can contribute to the drift. Comparing the drifts at different electron energies, the electric and magnetic drifts can be separated.

When emitted in the proper directions, the electron beam returns to dedicated detectors on the spacecraft after one or more gyrations. During these gyrations, the beam probes the ambient electric field at a distance from the spacecraft that for sufficiently small magnetic fields is essentially outside the latter's influence. In this paper we describe the basis of the method and the constraints imposed by the magnetic and electric field strengths to be encountered. We emphasize the criteria that led to the design of the Electron Drift Instrument (EDI) for the Cluster mission. EDI employs two electron guns, each of which can be aimed electronically in any direction over more than a hemisphere. A servo loop continuously re-aims the electron guns so that the beams return to dedicated detectors. The electron drift can be calculated by triangulation of the two emission directions. For small magnetic fields, the triangulation method becomes inaccurate, and the drift will instead be calculated from the measured differences in the time of flight of the electrons in the two nearly oppositely

[1]Max-Planck-Institut für extraterrestrische Physik, 85740 Garching, Germany

[2]University of California at San Diego, La Jolla, CA 94304, USA

[3]Lockheed Space Science Laboratory, Palo Alto, CA 92093, USA

[4]University of New Hampshire, Durham, NH 03824, USA

[5]University of Washington, Seattle, WA 98195, USA

Measurement Techniques in Space Plasmas: Fields
Geophysical Monograph 103

directed beams. The time-of-flight measurements also yield an accurate determination of the magnetic field strength.

The electron drift technique has a number of limitations. First, performance is strongly affected by the magnitudes of the fluxes of returning beam electrons and of ambient electrons. Second, measurements will be interrupted whenever the beam is strongly scattered by instabilities or interactions with ambient fluctuations. Third, beam tracking will be interrupted by very rapid changes in either the magnetic or the electric field. Fourth, accurate separation of the electric and magnetic components of the drift may not always be possible with only a limited range of electron energies.

2. PRINCIPLE OF OPERATION

2.1. Drift Velocity from Beam Direction Measurements

The basis of the electron drift technique is the injection of test electrons and the registration of their gyrocenter displacements after one or more gyrations in the magnetic field, **B**. The displacement, **d**, referred to as the drift step, is related to the drift velocity, $\mathbf{v}_D$, by:

$$\mathbf{d} = \mathbf{v}_D \cdot N \cdot T_g, \tag{1}$$

where T_g is the gyroperiod and N denotes the number of such periods after which the electrons are captured. If the drift is solely due to an electric field, $\mathbf{E}_\perp$, transverse to **B**, then (using MKSA units)

$$\mathbf{d} = \frac{\mathbf{E} \times \mathbf{B}}{B^2} \cdot N \cdot T_g. \tag{2}$$

Or, numerically, for $N = 1$

$$d\,(\mathrm{m}) = 3.57 \times 10^4 \frac{E_\perp\,(\mathrm{mV/m})}{B^2\,(\mathrm{nT})}. \tag{3}$$

Values of the drift step d as a function of magnetic field strength and drift velocity are shown in Figure 1.

The B^{-2} scaling implies that for a given electric field (1 mV/m, say), the drift step varies between 0.06 mm at low altitudes (25000 nT), and 1428 m in the solar wind or the central plasma sheet (5 nT), i.e., by a factor of $2.5 \cdot 10^7$. For small drift steps, the electrons gyrate nearly back to their origin and can be intercepted by a detector essentially collocated with the electron source. This is the scheme chosen for the Freja mission and described in another article in this monograph [*Kletzing et al.*, 1997]. The first application of the electron-drift technique was designed for the few-hundred nT fields

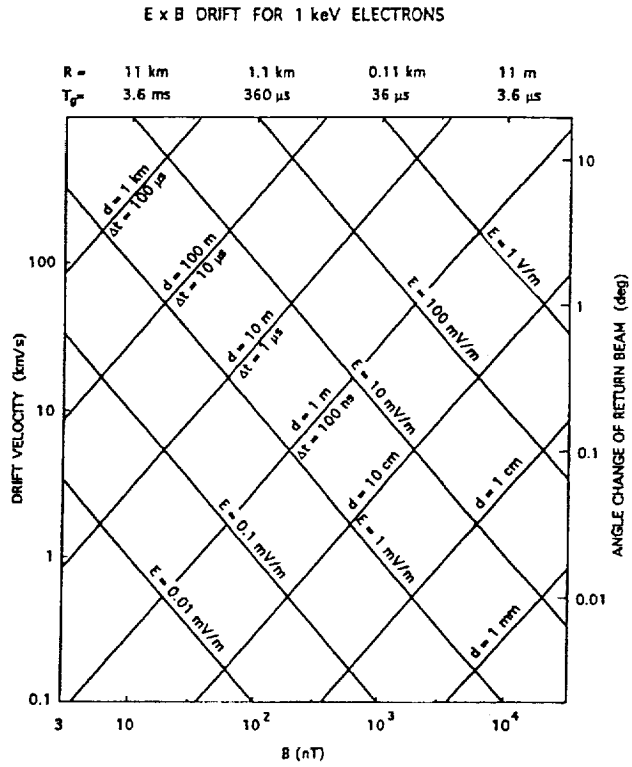

Figure 1. Magnitudes of the quantities directly measured by the electron drift technique, in terms of lines of constant drift step d and time-of-flight difference Δt, as a function of magnetic field strength and electron drift velocity, for 1 keV electrons. Lines of constant electric field are also provided. The electron gyroradius R and gyrotime T_g are indicated along the top, the angle change of the return beam along the vertical axis on the right.

at synchronous altitude [*Melzner et al.*, 1978] where the drift step can become much larger than the spacecraft dimensions. This is even more true for the Cluster (and Phoenix) missions where magnetic fields range from <1000 nT at perigee to only a few nT at apogee. These large drift steps require a totally different measurement concept, as discussed in the next subsection.

That electrons emitted by an electron gun mounted on a spacecraft can gyrate back to a detector on the same spacecraft, even if the drift step is much larger than the spacecraft dimensions, can be understood in two ways. Consider first the electron motion in a moving frame where there is no electric field (Figure 2). In this frame all electron trajectories are circles and return to the origin regardless of their emission direction. The spacecraft, on the other hand, now moves with the electron drift speed along a straight line that intersects the possible electron orbits in varying phases of their gyration. Now it is easy to see which electrons will hit the spacecraft: those that arrive at the intersec-

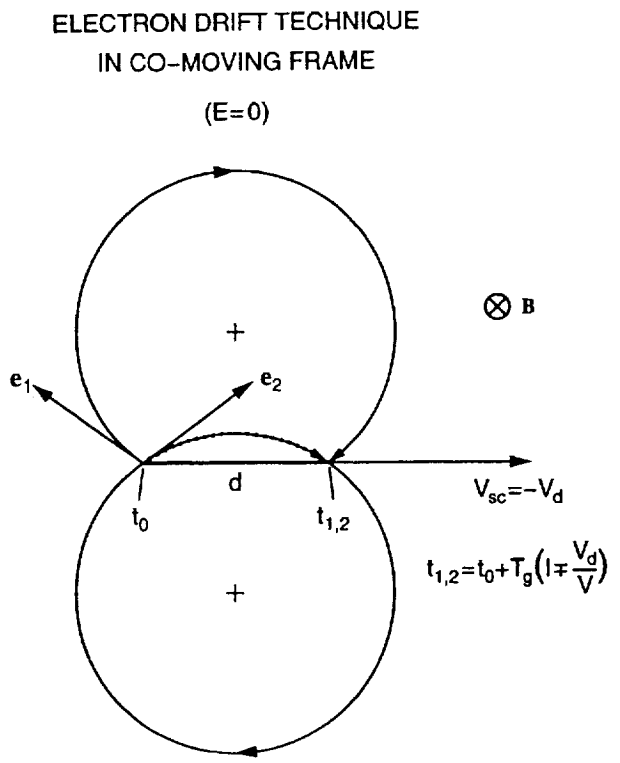

Figure 2. Principle of drift step determination in a coordinate system where there is no electric field. The arrows denoted e_1 and e_2 are the two gun pointing directions that cause the beams to hit the detector when it has moved to the point denoted $t_{1,2}$.

tion of their orbits with the spacecraft trajectory at the same time the spacecraft does. Two trajectories meet this requirement. To first order, these are the two circles (shown in the figure) whose secant is the distance (equal to the drift step) that the spacecraft moves in a gyroperiod. This is not quite correct; the upper trajectory has completed less than a full circle when it intersects the spacecraft trajectory, thus needing less than a gyroperiod, while the lower one needs more than a full gyroperiod. As a consequence, the true solutions are circles with emission directions that differ slightly from those shown, intersecting the spacecraft trajectory slightly left and right, respectively, of the single intersection shown in the figure. Note that the figure is for an unrealistically high ratio of drift step to gyroradius, and thus grossly exaggerates the difference between the two trajectories. For realistic ratios, the two have more nearly equal flight times, and emission directions that are closer to 180° apart. For the realistic case, the beam return directions are also more nearly parallel to the emission directions than shown in Figure 2.

While the co-moving frame is useful for explaining why there always are two trajectories that hit the spacecraft, considerations of the effects of the actual electron gun and detector geometry requires treatment in the spacecraft frame. For this we turn to Figure 3. First one notes that all electrons emitted from a common source S in a plane normal to **B** are focussed after one gyration onto a single point that is displaced from S by the drift step, **d**. The variability and size of the drift step makes it impossible to have an electron gun at S, and at the same time a detector D at the focus. But one does not really need a gun at S: a beam from a gun at an arbitrary location will also hit the detector at D, provided the beam is directed towards or away from S. In the first case the gun can be thought of as supplying electrons to the source at S, in the second the gun furbishes electrons emanating from the source. If two guns are used, as shown in the figure, determination of the beam emission directions that return a beam onto the detector yields the displacement, **d**, and thus the drift velocity, $\mathbf{v}_D$. This is a classical triangulation problem.

Of course, noting that the position of S is constantly changing in response to the varying electric and magnetic fields, finding the direction from each gun to the

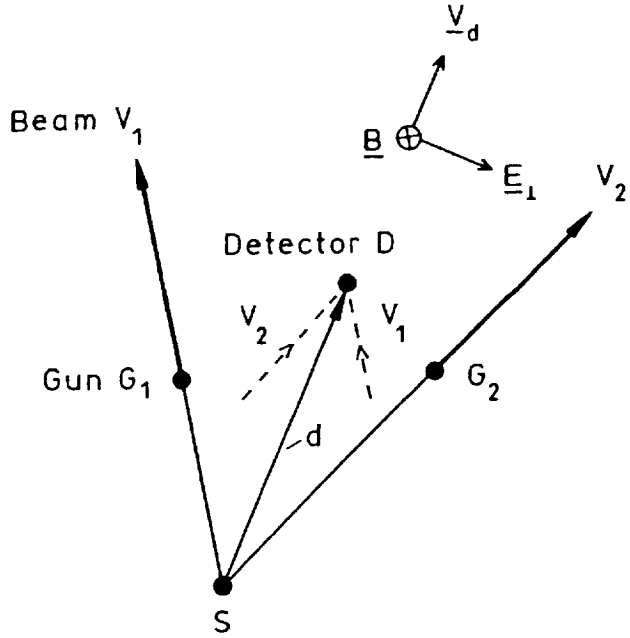

Figure 3. Principle of drift step triangulation in the spacecraft frame. If as a result of the drift all electrons emitted from S reach the detector location D after one gyration, then beams V_1 and V_2 directed along lines through S will also strike the detector. The drift step **d** is therefore the vector from the intersection point of the two beam directions to the detector D, once the beams are steered such that an 'echo' is received by the detector. Trajectories are straight lines in this figure because the drift step is assumed small compared with the gyroradius.

'target' at S (or away from it), and then keeping the beams on-target requires an active control of the beam pointing based on information from the detector.

As is true for any triangulation problem, the size of the baseline, b, and the beam pointing uncertainty determine the accuracy with which the displacement, **d**, can be measured. If the pointing accuracy of either beam is $\delta\alpha$, the error in the drift step is

$$\delta d = 2b\left(1+\frac{d^2}{b^2}\right)\delta\alpha \qquad (4)$$

The baseline is defined as the distance transverse to $\mathbf{v}_D$ between a gun and its associated detector when projected into the plane perpendicular to **B**. The maximum baseline is determined by the spacecraft diameter which in the case of Cluster is 3 m. As discussed below, for the gun-detector configuration used for the Electron Drift Instrument on Cluster, the effective baseline is actually twice as large, i.e., 6 m. Assuming a pointing accuracy $\delta\alpha$ of 0.5°, accuracies are better than 15% for drift steps <100 m. To determine larger drift steps one has to rely on measurements of the electron time of flight that are discussed in the next section.

The two beams return to the detector generally with substantially different directions. As detectors cannot view both these directions at the same time, one therefore needs a dedicated detector for each beam. Ideally, guns and detectors should not be co-planar, but rather form a tetrahedron. Otherwise there will be situations where the triangulation baseline vanishes, i.e., when **B** and $\mathbf{v}_D$ are in the gun/detector plane. Technical constraints ruled out such a solution on Cluster, and one gun and one detector were therefore combined in a single unit and two such gun-detector units mounted on opposite sides of the spacecraft. As a consequence, the triangulation baseline will vanish each time the projection of the two packages in the plane perpendicular to **B** is aligned with $\mathbf{v}_D$. Even though this will cause a spin-modulation of the accuracy with which the drift step is triangulated, the electron guns will stay on track. Note that in the worst case of a spin axis perpendicular to both **B** and $\mathbf{v}_D$, the baseline is always zero. Note also that with two detectors the triangulation scheme is modified as shown at the top of Figure 4, and becomes equivalent to one where the baseline is twice as large (bottom part of Figure 4).

With regard to Figures 3 and 4, note that when guns outside of S are used, D is no longer a focal point of the beams, nor do the travel times precisely equal the gyrotime, T_g. If the beam is directed towards (away from) the target S, the travel time will be longer (shorter) than T_g. This difference is the topic of the next subsection. Note also that electron trajectories are straight lines only if, as assumed in Figures 3 and 4, the drift step is small compared to the gyroradius. In the same approximation, the returning beams are parallel to the outgoing ones. Both approximations are no longer true for large drift steps. In this case the curvature of the electron orbits must be taken into account. The resulting effects were already discussed in conjunction with Figure 2.

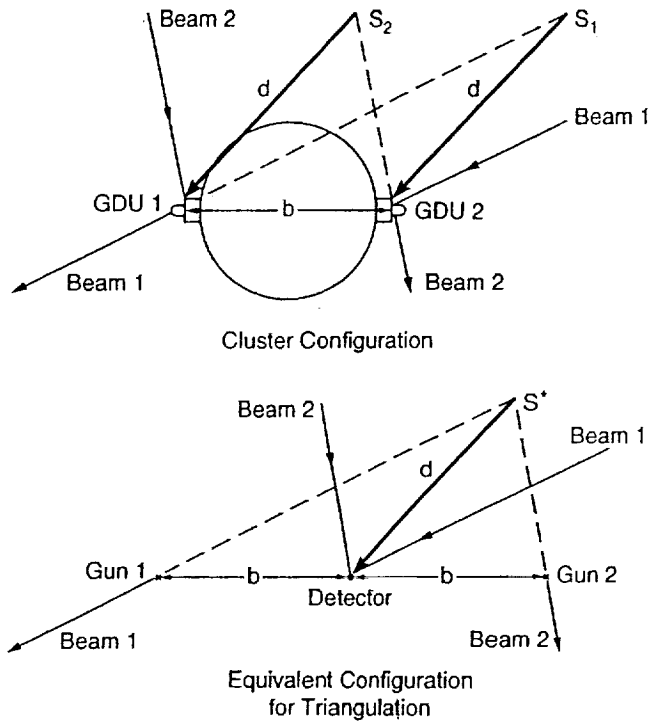

Figure 4. Triangulation scheme for two gun/detector units, GDU1 and GDU2, located on opposite sides of the spacecraft. S_1 and S_2 are the virtual source points for the two detectors (top). The problem is equivalent to one where a single detector is placed inbetween two guns at a distance b from each gun, and the virtual source becomes a single point, S^* (bottom). Note that the effective baseline is doubled this way.

Figure 5 shows the electron orbits in the spacecraft frame when one beam is directed towards the target, the other away from it. The differences in beam emission and arriving directions are clearly visible, as are the different trajectory shapes that imply differences in electron time of flight. The effects are highly exaggerated because the figure is drawn to scale for the case of a gyroradius of 9 m and a drift step of 3 m that imply magnetic and electric fields of 11.8 μT and 12 V/m, respectively.

The angle between outgoing and returning beam (in radians) is given by

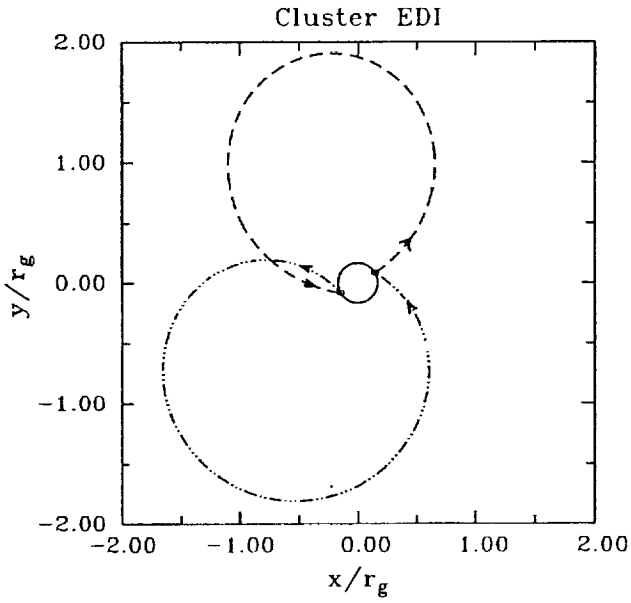

Figure 5. Electron orbits that return to detectors on the opposite side of a 3 m-diameter spacecraft, for a drift step of 4.5 m and a gyroradius of 9 m. These parameters were chosen so that spacecraft and orbits could be drawn to scale, but in fact are for unrealistically large magnetic and electric fields, namely 11.8 μT and 12 V/m, respectively. The magnetic field is pointing out of the page and the drift velocity is directed along X. The X and Y axes are scaled in gyroradii r_g.

$$\delta \approx 2\pi \frac{v_D}{v}, \tag{5}$$

where v is the electron speed which for 1 keV electrons is 18742 km/s. For drift speeds of 100 km/s and 1 keV electrons, δ is 1.9°, increasing to almost 10° at 500 km/s. This effect can complicate operation, because if δ exceeds the width of the detector angular acceptance, the detector viewing direction must be offset from the direction anti-parallel to the gun firing direction by an amount dependent on the quantity to be measured.

Before turning to the time-of-flight measurements, we should mention that in the original application of the electron-drift technique on the Geos spacecraft, a much simpler triangulation scheme was used that required only a single gun and no active control, at the expense of providing only a single drift-step measurement per spacecraft revolution. The Geos scheme is illustrated in Figure 6. Electrons emitted in a fixed direction are displaced by $S = d\sin\alpha$ after they have gyrated once, where α is the angle between beam and drift directions. Spacecraft spin causes α to cover the full range between 0° and 360° twice per spin. When α is such that $S = a$, where a is the gun-detector spacing, the beam will hit the detector. This condition is met twice per spacecraft spin. From the spin-phases when this occurs, the drift direction and magnitude can be reconstructed. The analysis assumes that the drift stays constant over times the order of the satellite spin period which for Geos was 6 s.

2.2. Drift Velocities from Time-of-Flight Measurements

As already illustrated in the previous section, the electrons in the two beams returning to the detectors travel different path lengths. As a result their flight times differ by an amount given by

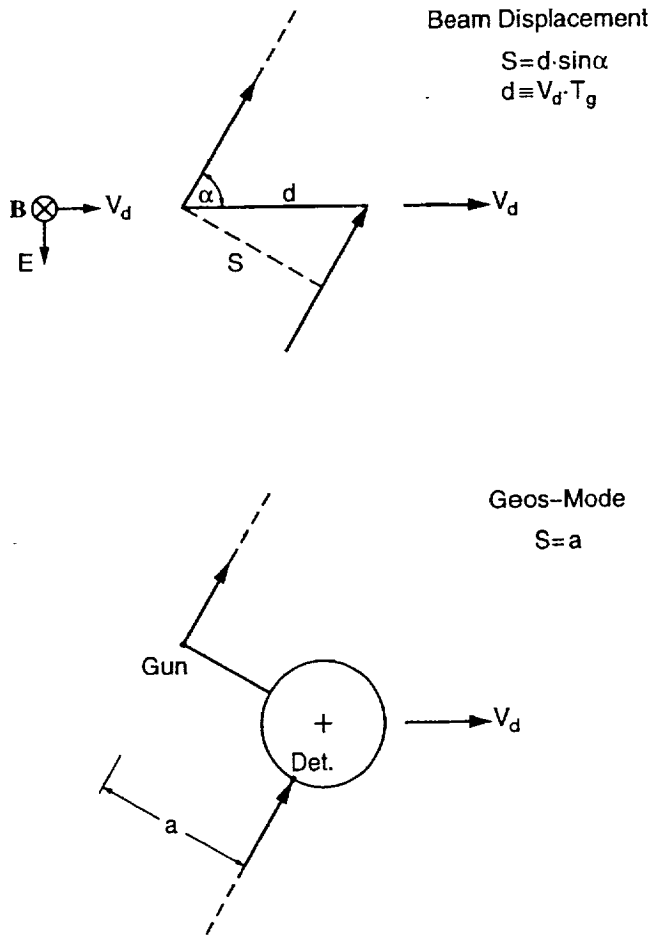

Figure 6. Beam displacement S as a function of the angle α between beam emission and drift velocity directions (top), and utilization of the variation of α with spacecraft rotation until S matches the gun-detector separation a, in the GEOS application of the electron drift technique (bottom).

$$\Delta T = T_{\rm to} - T_{\rm aw} = 2 \cdot T_g \cdot \frac{v_D}{v} \propto \frac{d}{v}, \qquad (6)$$

where $T_{\rm to}$ and $T_{\rm aw}$ are the flight times for the beam electrons aimed towards and away from the target, respectively. The idea to use electron times-of-flight to obtain the drift velocity is due to *Tsuruda et al.* [1985]. It has been successfully applied in the 'Boomerang' instrument on Geotail [*Tsuruda et al.*, 1994].

In the limit of very large drift steps, as depicted in Figure 7, the towards (away) beams are directed essentially anti-parallel (parallel) to the drift velocity. For simplicity it has been assumed here that guns and detectors are collocated, or in other words that the drift step is large compared to gun-detector separations.

The gyroperiod itself is obtained from the mean of the travel times:

$$T_g = \frac{T_{\rm to} + T_{\rm aw}}{2} \qquad (7)$$

Measuring $T_{\rm to}$ and $T_{\rm aw}$ permits determination of $\mathbf{v}_D$. ΔT scales directly as d/v. Hence, while the triangulation becomes increasingly less accurate, the time-of-flight method becomes more accurate with increasing drift step d, limited only by detector signal-to-noise effects. As shown in Figure 1, ΔT is many μs for those regions where the triangulation method starts to fail. Appropriate pulse-coding of the beams makes it possible to measure the time of flight of the electrons with a resolution better than 1 μs.

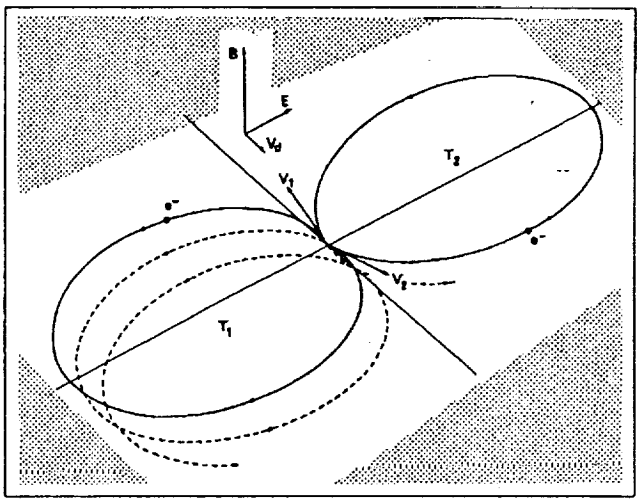

Figure 7. Principle of drift determination via time-of-flight measurements. Electrons emitted in a direction, v_1, opposing the drift, v_d, travel a longer path, and thus have a longer gyrotime, T_1, than electrons emitted along the drift, which take T_2 (from *Tsuruda et al.*, 1985).

2.3. Measurement of B

As discussed in the previous subsection, measurement of electron times of flight yields their gyroperiod, T_g, which in turn yields the magnetic field strength, B, via

$$T_g = \frac{2\pi m}{eB}. \qquad (8)$$

Values of T_g range from about 0.1 to 10 ms (see Figure 1) and are thus easily measurable. As a result, the magnetic field strength can be determined with very high accuracy, as demonstrated on Geotail [*Tsuruda et al.*, 1994].

2.4. Separation of Electric and Magnetic Gradient Drift

The beam electrons are subject not only to electric field drifts, but also to drifts caused by magnetic field gradients, $\nabla_\perp B$, directed perpendicular to the magnetic field. When the scale-length, ℓ, of such inhomogeneities becomes small (as it does at the bow shock, the magnetopause, or at the edges or the center of the plasma sheet), the gradient drift will make a significant contribution to the test electrons' displacement. The ratio of this drift, v_B, to that caused by the transverse electric field in the spacecraft frame of reference, v_E, is

$$\frac{v_B}{v_E} = 10^3 \frac{W_e\,(\mathrm{keV})}{E_\perp\,(\mathrm{mV/m})}\,\ell^{-1}\,(\mathrm{km}), \qquad (9)$$

where W_e is the energy of the electron. For 1 keV test electrons and a field of 1 mV/m, v_B/v_E reaches unity if ℓ approaches 1000 km. The equation suggests that to separate the two drifts, one should employ electrons at different energies.

When the total drift is measured at two energies, W_1 and W_2, with $r = W_2/W_1$, the electric and magnetic drifts are obtained from the following expressions:

$$\mathbf{v}_E = \frac{(r\mathbf{v}_1 - \mathbf{v}_2)}{(r-1)} \qquad (10)$$

$$\mathbf{v}_B(W1) = \frac{(\mathbf{v}_2 - \mathbf{v}_1)}{(r-1)} \qquad (11)$$

where $\mathbf{v}_1$ and $\mathbf{v}_2$ are the (total) drifts that are inferred from the triangulation analysis applied to the two measurements at energies W_1 and W_2, respectively.

When the time-of-flight measurement technique is used in the presence of a significant gradient in **B**, the analysis is more complicated. Since the gyrotime is defined in terms of the magnetic field at the center of the gyro circle, the two beams fired parallel and anti-parallel to the drift direction (Figure 7) will have differ-

ent gyrotimes. If there were only the $\nabla_\perp B$ drift (i.e., no electric field), then the gyrotimes are given by:

$$T_g = T_0 \left(1 + \frac{R_g \sin \Phi_0}{\ell}\right) \tag{12}$$

For the anti-parallel beam, $\Phi_0 = \pi/2$ and for the parallel beam $\Phi_0 = -\pi/2$, if one assumes that the gradient in **B** is in the same direction as **E** in Figure 7. Here T_0 is the gyrotime as given by the magnetic field at the spacecraft and R_g the corresponding gyroradius. The drift velocity and drift step are:

$$v_B = v_{B0} \left(1 + \frac{2R_g \sin \Phi_0}{\ell}\right) \tag{13}$$

$$d_B = d_{B0} \left(1 + \frac{3R_g \sin \Phi_0}{\ell}\right) \tag{14}$$

where again v_{B0} and d_{B0} are the values in terms of the magnetic field at the spacecraft. Use of the measured times now results in:

$$T_{\rm to} + T_{\rm aw} = 2T_0 \tag{15}$$

as before, but

$$\Delta T = T_{\rm to} - T_{\rm aw} = 6T_0 \frac{v_{B0}}{v_0}. \tag{16}$$

When both an electric field and a gradient in the magnetic field are present it can be shown that the difference in measured times for two beams fired anti-parallel and parallel to the net drift direction is given to leading order by:

$$\Delta T = T_0 \left(4 \frac{v_{B0}}{v_0} \sin \delta\Phi + \frac{2}{v_0} |\mathbf{v}_E + \mathbf{v}_{B0}|\right) \tag{17}$$

Here, $\delta\Phi$ is the starting angle of the anti-parallel beam with respect to the direction of the magnetic field gradient.

In general there are four unknown quantities: the magnitude and direction (or equivalently, the x and y components) of both $\mathbf{v}_B$ and $\mathbf{v}_E$ in the plane perpendicular to **B**. When two energies are used there will be six measured quantities: two net drift directions (one at each energy) and two pairs of flight times for the parallel and anti-parallel beams. However the flight times are not all independent since the sum of the pair for each energy is $2T_0$. Nevertheless the net drift directions and the differences in measured flight times for the two energies provide four relations that make it possible to obtain the four unknown drift components of $\mathbf{v}_B$ and $\mathbf{v}_E$.

3. CONCEPTUAL DESIGN CRITERIA

In this section we focus on the parameters that determine instrument conceptual design, with emphasis on the application for the Cluster mission. A technical description of the Electron Drift Instrument for Cluster has been published elsewhere [*Paschmann et al.*, 1997].

3.1. Beam Return Fluxes

A key design criterion for the electron drift measurements is the magnitude of the flux of returning electrons incident on the detectors. This flux depends upon many factors, including the angular current distribution of the outgoing beam, the beam gyroradius, possible beam modification by electrostatic or wave-particle forces, and the geometrical arrangement of the gun and detector with respect to the drift step vector. The outgoing beam has an opening angle, β, of approximately 1°. Thus the beam diverges along the magnetic field direction by a distance $s_\parallel = 2\pi R_g \beta/57.3$, where R_g is the gyroradius, but is focussed in the plane perpendicular to **B** after one gyro orbit. By definition, this focus is located one 'drift step' from the gun. In general, those beam electrons with the proper firing direction encounter the detector either somewhat before, or somewhat after, this focus point. Thus the beam divergence leads to a large variation in the return beam flux with magnetic field strength and drift step. If gyro radius and drift step are as large as encountered on Cluster (see Figure 1), the detector intercepts only a small part of the emitted beam. Large detector sensitivity and particle counting techniques are necessary under such conditions. For the Freja application where gyro-radius and drift step are small, the return fluxes are large enough so that simple detection schemes are feasible [*Kletzing et al.*, 1997].

Equation 18 gives the beam flux, F, in $\mathrm{cm^{-2}s^{-1}}$, at the detector for an emitted beam with a flat current distribution over a square angular cross-section, where I is the gun current in nA, B the magnetic field strength in nT, W the beam energy in keV, x the distance from the gun's gyrofocus to the detector in m, β the beam full width parallel and perpendicular to **B** in degrees, and R_g the gyroradius in m.

$$F = 3.1 \cdot 10^3 \frac{IB}{x\beta^2 W^{1/2} (1 \pm x/2\pi R_g)} \tag{18}$$

The $\pm$-term in the denominator accounts for divergence parallel to **B** between the gun's gyrofocus and the detector, depending upon whether the detector intercepts the beam before $(-)$ or after $(+)$ the gyrofocus.

Of course a square, uniform cross-section is not a realistic representation of the actual beam. However for that portion of the real beam that has the same angular current density I/β^2 as the uniform beam, the return flux at the detector would be the same.

Note that above equation is for electrons having gyrated once. For electrons having gyrated N times, the return flux scales as $1/N^2$.

3.2. Requirements on Gun and Detector Designs

For applications in weak magnetic fields, the electron drift measurements require electron guns capable of providing a beam that can be steered rapidly into any direction within more than a hemisphere. Electron energies must be variable in order to separate $\mathbf{E} \times \mathbf{B}$ and $\nabla_\perp B$ drifts. At the same time the energy dispersion must be small to restrict beam spreading in space and time. Beam currents must be variable between 0.1 nA and more than 1000 nA to account for the strong dependence of return fluxes on B and E. To maximize the return signal in the detectors and to provide accurate triangulation, the angular width of the beam must be kept small, but still large enough to account for uncertainties in pointing direction. The pointing accuracy must be 0.5° or better in order to extend the triangulation measurements to large enough drift steps that electron time-of-flight measurements can take over. The time-of-flight measurements in turn require that the beam be modulated and coded.

To detect the electrons from the two beams one needs two detectors. Each detector must be able to look in any direction within a region greater than a 2π steradian hemisphere. To follow the rapidly changing beam return directions, the detectors must be capable of changing their look directions in less than a millisecond. The detectors must have a large effective area, as much as two or three square centimeters, to guarantee adequate count rates under conditions when the return fluxes are weak. At the same time sensitivity to electron fluxes from the ambient plasma must be suppressed as much as possible to provide adequate signal-to-noise ratios. Unlike the ambient electrons, the returning beam is monoenergetic and unidirectional. Therefore, the signal-to-noise ratio is improved by designing the detector to be selective in velocity space. By changing the width of the accepted energy band and the focussing properties of the detector optics, one can choose different combinations of the sensitive area and angular acceptance width for beam electrons on the one hand, and the geometric factor for ambient electrons on the other hand. This is achieved by properly choosing the voltages on the electrodes in the detector optics. We refer to the different combinations as detector 'states'. Choice of the detector 'state' is to be based on beam fluxes and signal-to-noise ratio considerations.

3.3. Beam Recognition, Tracking and Coding

To detect the beam electrons in the presence of background counts from ambient electrons, and to measure their flight time, the electron beam is intensity modulated with a pseudo-noise code (PNC). The modulation frequency must reflect the expected time delays and the desired delay-time accuracy, and for EDI on Cluster can be chosen between 8 kHz and 4 MHz. The stream of electron event pulses received by the detectors are fed in parallel into an array of counters ('correlators'), each one gated with its individual copy of the PNC, shifted by one chip from counter to counter, and delayed as a whole (by a variable amount) against the PNC used to modulate the outgoing beam. The correlator that is controlled by the PNC matching the flight time will receive the most signal counts. For details concerning the correlator design, we refer the reader to the paper by *Vaith et al.* [1997].

We have experimented with several correlator schemes. The one presently implemented uses a 15-chip pseudo-noise code and 15 correlator channels. It guarantees that beam electrons are always counted in one of the channels, regardless of flight time. But it has the disadvantage that the flight time is determined only modulo the code duration and thus can be ambiguous. Electrons having gyrated more than once can also not be uniquely distinguished from the electrons having gyrated once. The ambiguity in flight time can usually be removed by starting out with a sufficiently low code-clock frequency such that the entire range of expected flight times fits within one code-length. This initial frequency is based on the gyrofrequency computed from the magnetometer data and an assumed 10% variation in flight-time to account for large electric fields.

In the standard mode of operation foreseen for the instrument on Cluster ('Windshield-Wiper Mode'), both beams are swept in the plane perpendicular to $\mathbf{B}$ in 0.25°-steps every ms. After every step, the signal-to-noise ratio is computed from the maximum and minimum counts in the set of 15 correlator channels associated with each detector. If that ratio exceeds some (selectable) limit, this is an indication that the beam is striking its detector. The angular sweep is continued until the signal is lost, i.e., the beam has completed its pass over the target. When this happens, the beam sweep direction for the gun in question is reversed and

the process repeated. The same procedure is followed for the other gun. This way both beams are independently sweeping back and forth over the target. Beam currents and detector 'states' are continuously adjusted to maximize signal and/or signal-to-noise.

If the beam were always returning parallel to its emission direction, it would be sufficient to simply steer each detector to look at a direction anti-parallel to the emission direction of the associated beam. But as we have seen above, there is an angle δ between the two directions. As long as δ is less than the acceptance angle of the detector, this does not cause any problem. We therefore use detector optics 'states' with large acceptance angles for target acquisition. Once signal has been acquired, δ can be computed from the time-of-flight differences between the two beams. This allows switching over to a detector state with better signal or signal-to-noise properties, but narrower acceptance angle by offsetting the detector look-direction according to the sign and magnitude of δ.

4. CAPABILITIES AND LIMITATIONS OF THE TECHNIQUE

The electron drift technique primarily measures the electron drift velocity, from which the electric field perpendicular to the magnetic field, $\mathbf{E}_\perp$, including its component along the spacecraft spin axis, can be derived. By contrast, the double-probe technique usually measures $\mathbf{E}_\perp$ in the plane of the wire booms only. Under favorable conditions, it may also be possible to infer $\mathbf{E}_\parallel$ from electron drift measurements. If local magnetic field gradients, $\nabla_\perp B$, contribute significantly to the electron drift velocity, the electron drift technique provides the unique capability of determining these local magnetic field gradients from a comparison of the electron drift at different energies. When electron time-of-flight measurements are made, the technique also yields accurate measurements of the magnetic field strength, B.

The quantities directly measured by the electron drift technique all scale with some power of the ambient magnetic field strength B. For a given electric field E, the drift step and the time-of-flight difference scale as B^{-2}, the return flux as B^3, and the angle between beam emission and return directions as B^{-1}. In addition, the electron gyroradius which determines the scale over which the measurements are made, scales as B^{-1}. Figure 8 summarizes the scaling relations in terms of B, E, and the electron speed v. Because of the strong B-dependence, the expected values of B very much determine whether triangulation or time-of-flight techniques

EDI SCALING

$$d \equiv v_d \cdot T_g \propto \frac{E}{B^2}$$

$$T_{1/2} \equiv T_g \left(1 \pm \frac{v_d}{v}\right)$$

$$T_2 - T_1 = 2\, T_g \frac{v_d}{v} \propto \frac{E}{B^2}$$

$$T_g = \frac{T_1 + T_2}{2}$$

$$\text{Flux} \propto I_B \cdot \frac{B^3}{E} \frac{1}{v}$$

$$\delta \propto \frac{E}{B} \frac{1}{v}$$

Figure 8. Scaling relations for the quantities that characterize the electron drift technique: drift step d; electron time-of-flights and their difference T_1, T_2, and $T_2 - T_1$; gyrotime T_g; return beam flux; and angle change δ of return beam.

are applicable and what complexity in the gun and detector designs is required.

For example, if B is high, such as on low-altitude spacecraft, the drift step is so small that the beam always returns very close to its origin and the return fluxes are so large that simple detection techniques are feasible and the drift step is directly measured. Electrons gyrating more than once are no concern because they can be easily intercepted. On the other hand, gyrotimes are so small that time-of-flight measurements are not feasible. As a result, B is not measured under these circumstances. There is also the problem that the gyroradius can become so small that spacecraft effects cannot be ignored.

If B covers the range from very small to medium, such as on Cluster, time-of-flight measurements of the drift velocity are feasible, and B is thus measured as well. Spacecraft effects are of little concern because the

gyro-radius is large. On the other hand, because of the large size of the drift step, the gun-detector geometry must be carefully chosen, and the beam firing directions must be actively controlled. Large gyroradius and drift step conspire to make the beam return fluxes generally small even for the largest feasible beam emission currents. This together with the presence of large fluxes of background electrons from the ambient plasma, requires elaborate detectors and correlation techniques to compensate for the low signals and/or low signal-to-noise ratios. On the other hand, when B increases, and thus the gyro-radius and drift step become smaller, the fraction of the beam electrons that return becomes larger and larger, eventually requiring a reduction in beam current in order not to saturate the detectors. Thus beam emission currents must be constantly adjusted. The implied large variations in signal-to-noise ratio affect the achievable time resolution of the measurements and can lead to loss of track.

To instantaneously separate electric and magnetic components of the electron drift, one would ideally want two fully redundant gun-detector systems and associated control, operating at widely different energies. Because resource limitations ruled out such a solution on Cluster, we use the same system to sequentially operate at the two energies which the design supports, namely 0.5 and 1.0 kev. A factor of two in beam energy will not always be sufficient to separate the drifts. Furthermore, variations in the fields on the time-scale of the energy variation will also cause difficulties.

In addition to the constraints already noted, the electron drift measurements can be adversely affected by intrinsic beam instabilities, strong scattering of the beam by ambient fluctuations, large-amplitude 'spikes' in the electric field, and very rapid magnetic field variations. All these effects can cause a loss of beam track and thus a momentary loss of data.

While the electron drift measurements might at times be compromised, there is another measurement capability that enhances the scientific return from such an instrument at no extra cost: the ability to make unique measurements of ambient electron and ion distributions, thanks to the special properties of the detectors and their control. Each of the two detectors can be commanded to look in any direction over greater than a 2π steradian hemisphere, and since the two detectors are mounted on opposite sides of the spacecraft, full-sky surveys can be achieved without relying on spacecraft spin to complete the coverage of phase space. In addition, since much of the control is already based on the **B** field measured by the on-board magnetometer, specialized surveys can be performed in coordinates fixed with **B**, and they can be performed continuously.

REFERENCES

Kletzing, C.A., G. Paschmann, and M. Boehm, Electric field measurements using the electron beam technique at low altitudes, 1997 (this volume).

Melzner, F., G. Metzner, and D. Antrack, The Geos electron beam experiment, *Space Sci. Rev.*, **4**, 45, 1978.

Paschmann, G., F. Melzner, R. Frenzel, H. Vaith, P. Parigger, U. Pagel, O.H. Bauer, G. Haerendel, W. Baumjohann, N. Sckopke, R.B. Torbert, B. Briggs, J. Chan, K. Lynch, K. Morey, J.M. Quinn, D. Simpson, C. Young, C.E. McIlwain, W. Fillius, S.S. Kerr, R. Maheu, and E,C. Whipple, The electron drift instrument for Cluster, *Space Sci. Rev.*, **79**, 233, 1997.

Tsuruda, K., H. Hayakawa, and M. Nakamura, in A. Nishida (ed.), *Science Objectives of the Geotail Mission*, ISAS, Tokyo, p. 234, 1985.

Tsuruda, K., H. Hayakawa, M. Nakamura, T. Okada, A. Matsuoka, F.S. Mozer, and R. Schmidt, Electric field measurements on the Geotail satellite, *J. Geomag. Geoelectr.*, **46**, 693, 1994.

Vaith, H., R. Frenzel, G. Paschmann, and F. Melzner, Electron gyro time measurement techniques for determining electric and magnetic fields, 1997 (this volume).

C. E. McIlwain, Center for Astrophysics and Space Science, University of California at San Diego, La Jolla, CA 94304, USA (e-mail: cmcilwai@ucsd.edu)

G. Paschmann, Max-Planck-Institut für extraterrestrische Physik, P.O.Box 1603, D-85740 Garching, Germany (e-mail: gep@mpe-garching.mpg.de)

J. M. Quinn, Institute for the Study of Earth, Oceans and Space, University of New Hampshire, Durham, NH 03824,USA (e-mail: jack.quinn@unh.edu)

R. B. Torbert, Institute for the Study of Earth, Oceans and Space, University of New Hampshire, Durham, NH 03824, USA (e-mail:torbert@unhedi1.unh.edu)

E. C. Whipple, Geophysics Department, Box 351650, University of Washington, Seattle, WA 98195, USA (e-mail: whipple@geophys.washington.edu)

Instrument Status

- Commissioning complete.
- One-month commissioning suspension, caused by s/c commanding problem, delayed optimization of operating algorithms.
- Successful beam tracking with both gun-detector pairs on all spacecraft.
- Excellent sensitivity demonstrated in test of CSDS data products.
- Investigating adjustments to beam current levels and pseudo-noise-code frequencies to reduce interference with wave instruments.
- Optimizing onboard IEL calibration and offsets to improve tracking at low B.

EDI Technique

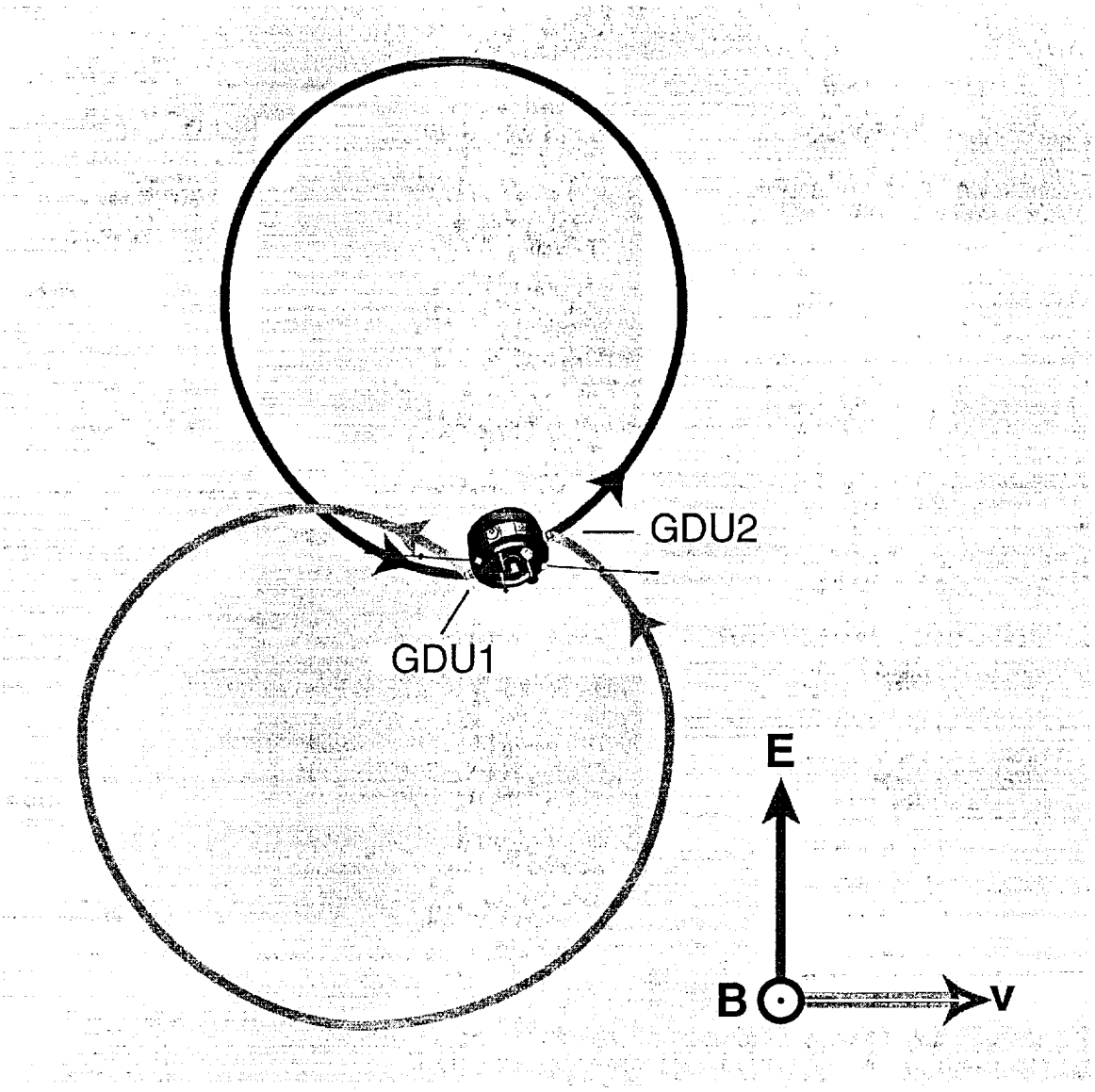

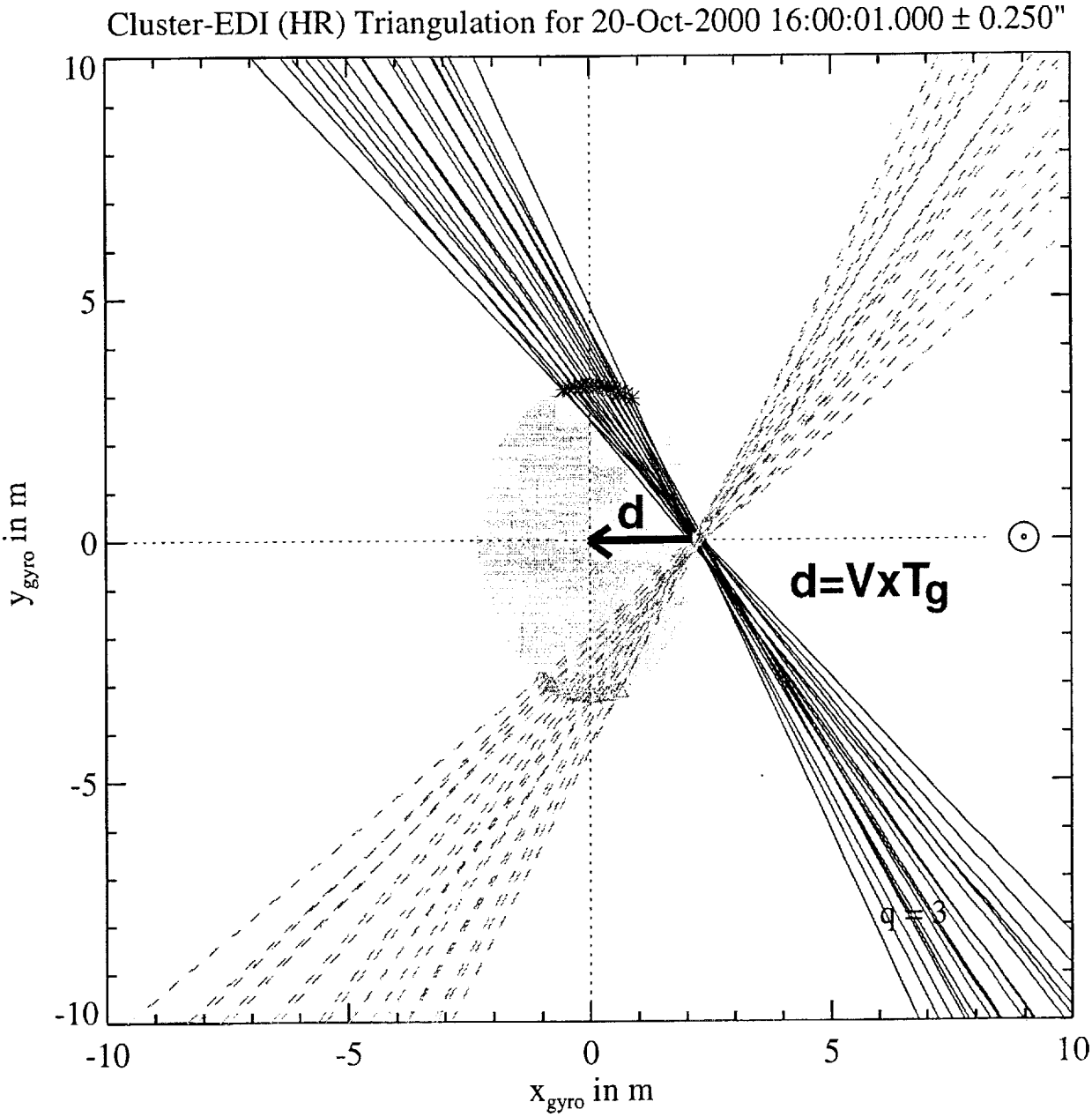

Straight-line approximation.

S/C projection and gun positions scaled by a factor of 2, virtual detector at center:

Beam crossing point ⇒ detector is the plasma drift per gyro period, **d**, in m.

Cluster-EDI 20-Oct-2000 SC-3

0.5 s Intervals at 10 Minute Spacing

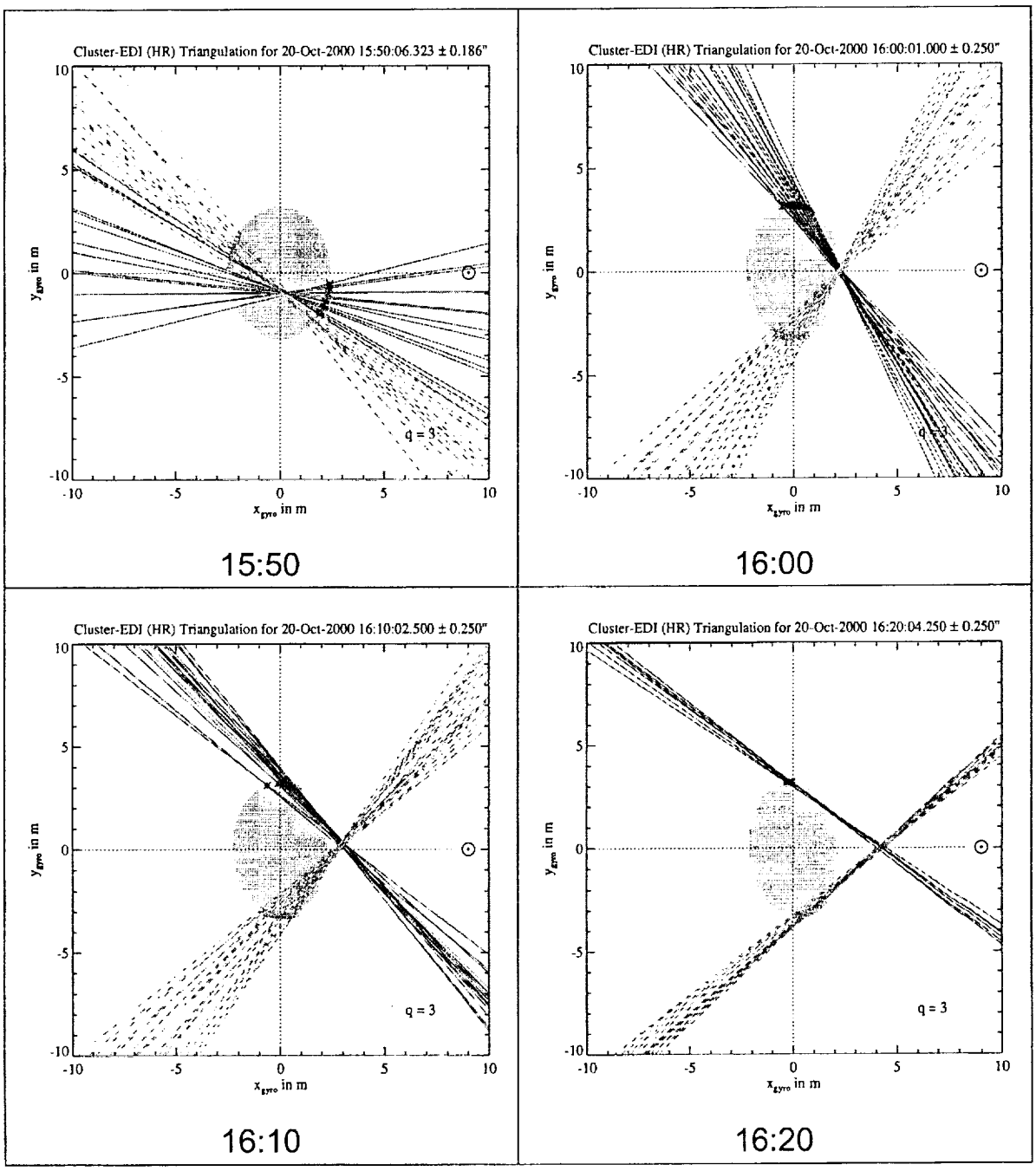

Anomalies

- Excess electron beam currents:
  - Anomalously high emitted beam-currents for 30-45 minute period following WW start-up, after which problem ceases.
  - 6 occurrences, including simultaneously on 3 s/c 9-Jan-2001.
  - HK values show growing error-currents, then sharp recovery.
  - Cause and correction under investigation.

- Instrument over-current:
  - 28V primary current sudden increase to exceed 370 mA limit.
  - Limited evidence indicates problem is gun-related.
  - Jan. 16, 19 software uploads for GDU-specific current monitoring and improved diagnostics.
  - Tests on SC-4 to further isolate problem

Initial Results

- Sensitive electric field measurements w/ good multi-s/c agreement
- ~ 200 beam "hits" per spin in some regimes;
  optimization continuing for low magnetic fields
- Spin-axis component of electric field measured with high sensitivity
- Independent determination of absolute magnetic field direction and magnitude

Electron Drift Instrument (EDI)
E_x [mV/m, SCS]

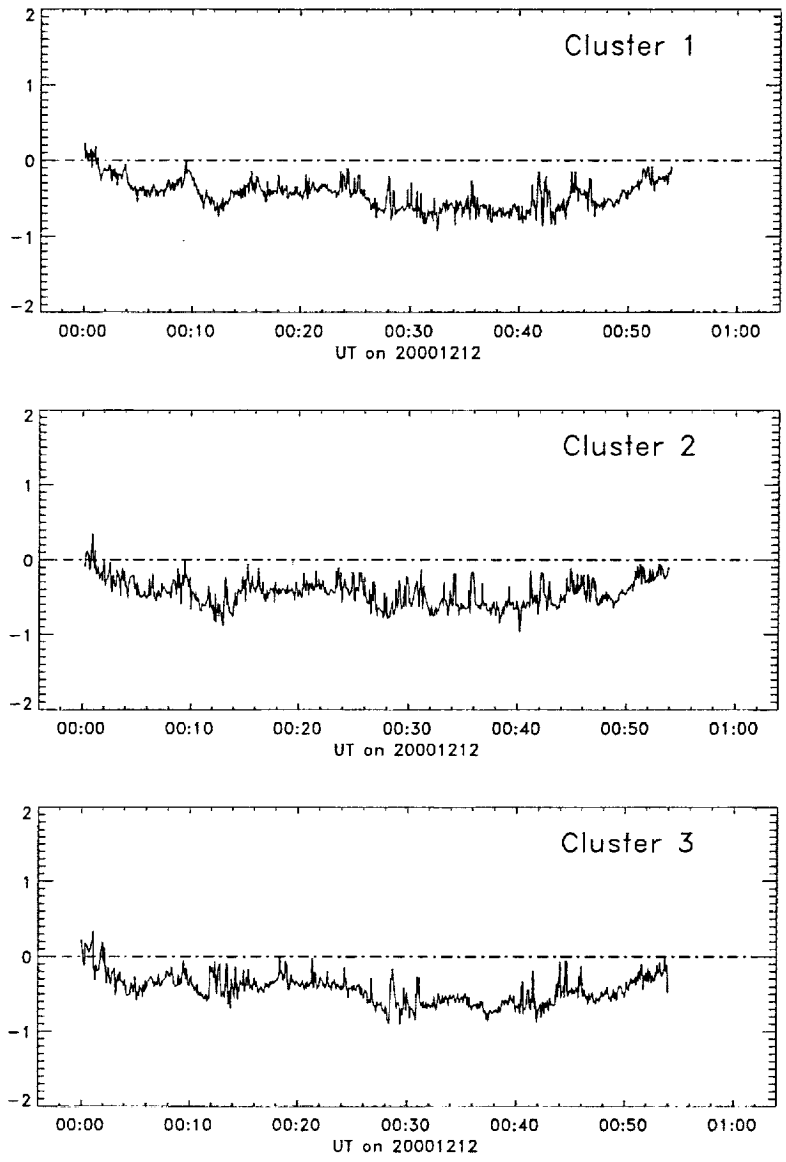

Electron Drift Instrument (EDI)
E_y [mV/m, SCS]

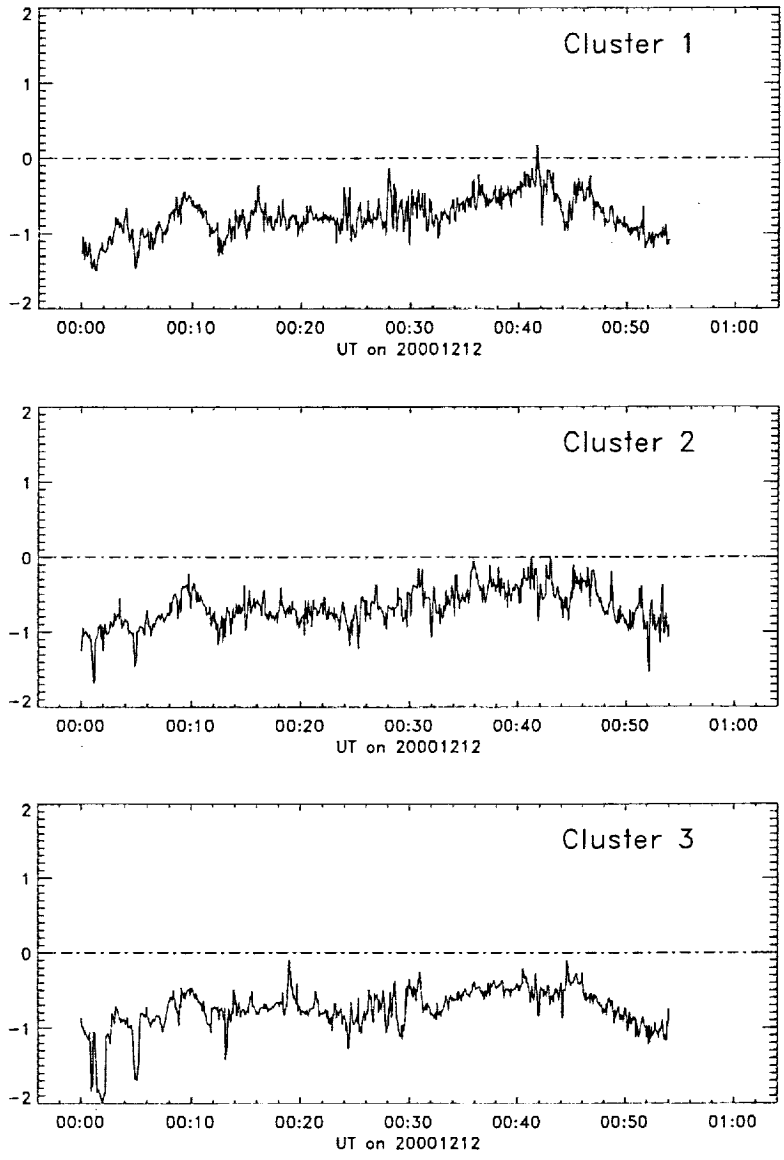

Electron Drift Instrument (EDI)
E_z [mV/m, SCS]

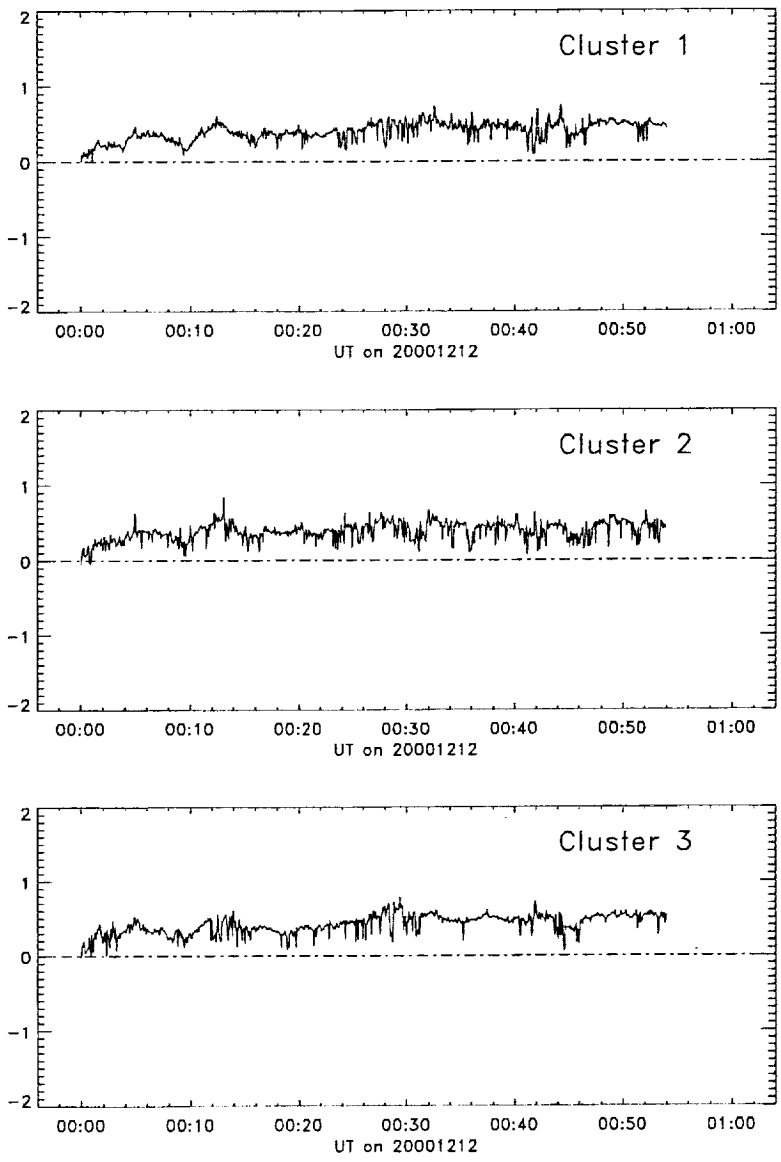

Mission Operations Readiness

- EDI is ready for the mission operational phase.
- Optimization of control parameters will continue.